



Theoretical and experimental analyses of vibration impulses and their influence on accurate diagnosis of ball bearing with localized outer race defect

Sameera Mufazzal^{a,*}, SM Muzakkir^a, Sidra Khanam^b

^a Department of Mechanical Engineering, Jamia Millia Islamia, New Delhi 25, India

^b Department of Mechanical Engineering, ZH CET, Aligarh Muslim University, Aligarh, India



ARTICLE INFO

Keywords:

Dual impulse
Multi-impact events
Point defect
Sinking depth
Varying compliance vibration

ABSTRACT

This work presents an in-depth analysis of vibration response of ball bearings using a modified 2-degree of freedom (DOF) lumped parameter model. It incorporates additional deflection and multi-impact theories to closely simulate the behavior of healthy and defective bearings, under different load and speed values. The varying compliance vibration has been studied in detail and it is found that the location and the number of impulses due to varying compliance strongly depend on multiple factors, and mainly on the values of applied load and shaft rotational speed. These impulses may merge with the actual defect induced impulses and can alter its characteristics. Moreover, the strengths of these impulses are comparable with those of defect induced peaks, especially for faults at incipient stage. It is illustrated that how the existence of these peaks due to varying compliance may build a misleading impression of the existence of outer race defect even when the bearing is totally healthy. Further, there are cases, in which the defective bearing does not even exhibit the dual vibration impulses. The fault identification and defect size estimation done directly on the ground of these impulses without a prior knowledge of their actual cause, could bring the operator to highly non-optimal decisions.

The numerical simulations have been conducted at different speeds, loads, defect sizes and locations, for investigating the influence of these parameters on the bearing response characteristics. Experimental results and detailed analyses are reported in this paper to support the proposed model and validate the numerical results.

1. Introduction

Rolling element bearing, being an indispensable element of most of the industrial rotary machines, requires continuous health monitoring to avoid any system failure and prevent unnecessary machine halts, production delays and the associated monetary losses. When the bearing witnesses an emerging fault, the dynamic response of the rotary system gets changed. In order to predict the internal status of the bearing and prevent unplanned outages by accurately scheduling the replacement activities, it has become a common practice to collect measurable response parameters, in the form of vibration, acoustic, temperature, oil contaminant, etc., and analyze these data to find the bearing fitness. These approaches certainly help the operators to gain an insight of the bearing health status and

* Corresponding author.

E-mail addresses: samechphy@gmail.com (S. Mufazzal), smmuzakkir@jmi.ac.in (S. Muzakkir), sidra.khanam10@gmail.com (S. Khanam).

Nomenclature

Critical Points

O	Center of the bearing
O_B	Center of ball
O_D	Defect center
$O_{l,t}$	Center of the curvature of the defect edge at leading/trailing ends
P_l	Instantaneous location of ball raceway contact patch inside the defect zone
$P_{s,e}$	Inflection point at start/end of the defect

Bearing parameters and geometry

ϕ_s	Angular spacing between the balls (rad)
ψ	Angular location of cage (or ball 1) with respect to the load line (rad)
D_p	Pitch diameter of ball bearing (m)
p_d	Diametral clearance (m)
R_b	Ball radius (m)
R_i	Inner race (IR) radius (m)
R_o	Outer race (OR) radius (m)
Z	Number of balls in the bearing

Defect parameters

α	Angular location of defect center with respect to the load line (rad)
β	Instantaneous angle between the location of the ball centre with respect to the bearing center and the line joining the ball center and the point O_l (rad)
θ_d	angular span of the defect about the bearing center (rad)
η	angular span of the defect about the center of the ball located in the defect (rad)
ψ_l	Angular location of point P_s with respect to the load line (rad)
a_d	Defect length (m)
f_{OR}	OR fault frequency (Hz)
h_d	Defect depth (m)
r_d	Defect edge radius (m)

Bearing kinematics

ω_b	Ball angular speed outside the defect zone (rad s^{-1})
ω_c	Angular speed of cage (rad s^{-1})
ω_f	Angular velocity of ball about the leading edge prior to impact (rad s^{-1})
ω_s	Angular speed of shaft (rad s^{-1})
F_{imp}	Impact force at exit edge (N)
F_r	Applied radial load (N)
J	Moment of inertia of ball (Kg m^2)

Ball raceway contact parameters

δ	Total angular deflection of the ball center (m)
F, ϵ	Complete elliptic integral of first/ second kind of contact ellipse (m)
κ	Ellipticity parameter of elliptic contact
E'	Effective modulus of elasticity (N m^{-2})
F_{ci}	Contact force at IR-ball contact (N)
F_{co}	Contact force at ball- defect edge contact (N)
h_s	Ball sink (m)
K	Hertzian contact stiffness (N m^{-1})
K_n	Load deflection (Hertzian) constant ($\text{N m}^{-1.5}$)
N_{LZ}	Number of balls in load zone
R	Effective radius of curvature at contact (m)
R_x	Effective radius of curvature at contact in the direction of motion (m)

Shaft and housing properties

$c_{s,h}$	Material damping of shaft/ housing (N s m^{-1})
m_s	Effective mass of shaft and IR at test bearing (kg)
m_h	Mass of housing and outer race (kg)
$k_{s,h}$	Stiffness of shaft/ housing (N m^{-1})

Motion parameters

$x_{s,h}$	Displacement of shaft/ housing along the load line (m)
$\dot{x}_{s,h}$	Velocity of shaft/ housing along the load line ($m s^{-1}$)
$\ddot{x}_{s,h}$	Acceleration of shaft/ housing along the load line (ms^{-2})
$x_{c,max}$	Maximum ball -raceway compression at the end of impact (m)

Oil film damping parameters

ξ	Pressure viscosity coefficient of lubricant ($m^2 N^{-1}$)
η_0	Oil viscosity at atmospheric pressure ($N s m^{-2}$)
c_e	Oil film damping due to squeezing effect ($N s m^{-1}$)
h_{min}	Minimum thickness of oil film at contact (mm)
H_{min}	Dimensionless minimum film thickness parameter
G	Dimensionless material parameter
U	Dimensionless speed parameter
u_x	Mean surface velocity in the direction of motion ($m s^{-1}$)
W	Dimensionless load parameter

track the emergence of defect soon it enters the system, however in order to correctly understand these features and effectively correlate the changes/ trend in these parameters with actual bearing internal condition by relying on the natural occurring faults, will be definitely a non-feasible approach. In such situations, the response model can be beneficial for approximate simulation of the system behavior under varying operating conditions. Nevertheless, not all, but only reasonably accurate model, which can closely reproduce the response characteristics of the system, can help the operators reach the root cause of failure. These models are also increasingly becoming important as they are emerging as a source of interpretation of signals, which are required for accurate fault diagnosis. Once an accurate fault diagnosis is complete, the integration of the acquired results with an appropriate defect growth model can result in establishment of a reliable as well as an economic maintenance framework. Due to these reasons, many researchers in the past have attempted to simulate the response of the system due to complex static and dynamic behavior of the bearings, arising out of non-linear contacts between different mating components and various tribo-mechanical events [1], including slipping between the mating components [2], both for healthy and defective bearings. The research in bearing fault modeling has been active since more than past three decades due to which intractable number of literatures is available to date. Hence, the present section briefs a review of the only very relevant theoretical models, which were developed to simulate the behavior of rolling element bearing with localized defect.

Cao et al. [1] have recently published a detailed review of all the major mechanical models of rotor-bearing system and categorized them into five major types as: lumped parameter, quasi-static, quasi-dynamic, dynamic, and finite element based models. Further, for bearings with localized defect, a brief review of the mathematical models carried out by Shah and Patel [3] can be referred to gain a quick insight of the subject.

McFadden and Smith [4] were the first to model the vibration response of the bearing with single point defect on inner race (IR) in the form of defect impulses, repeating at characteristic defect frequencies. This model was next extended by McFadden and Smith [5] to the bearings with multiple point defects on inner race. Epps [6] introduced the concept of multi-event excitation as the rolling element passes across the defect, and these events relate to the entry, impact, and the exit from the defect. Identification of these events can ultimately help in correlating the defect size with the signal data points sampled between the entry and the impact events. The similar observation of multi-event spikes in the vibration signal waveform was later reported by other researchers also [7–9].

Tandon and Choudhary [10] proposed a model to determine the defect frequencies and their amplitudes due to localized defect on outer race (OR), IR and on single rolling element, under the action of radial and axial load. The defects were modeled as finite width pulses of different shapes, and the effect of each shape was studied. Sopanen and Mikkola [11] formulated a 6-degree of freedom (DOF) model of bearing with localized defect while considering the waviness effect on the response of the system. The ball-raceway contact deformation was modeled using Hertzian non-linear theory. Moreover, the effects of lubricant film at the contacts, the internal clearance and the unbalance, were also incorporated. David Brie [12] proposed a quasi-periodic impulse train model for defective bearing, considering slip at the contacts and uncertainty associated with instantaneous contact angle calculations.

Rafsanjani [13] carried out linear stability analysis of rolling bearing rotor system containing bearing with local surface defects on raceways and rolling element, by modeling them as a nonlinear 2-DOF system. Sawalhi and Randall [7] combined the defective bearing model with the gear model to simulate the interaction between the gears and bearings of a gearbox. The bearing was represented as a 5-DOF system, with defects on inner and outer races, and on rolling elements. The rolling elements were considered as point masses and their paths in the defect were assumed based on the defect shape. The effect of 1–2% slip in shaft speed was incorporated in the model. In order to remove the need of assuming rolling element path, this work [7] was later modified by Ahmadi et al. [14] by considering finite size rolling element and finding the actual defect geometry.

Ashtekar et al. [15] obtained force-deflection relationship of bearing from the Hertzian model by modeling the spalls as surface dents. Choudhary and Tandon [16] proposed a 3-DOF lumped-mass vibration model to represent the complete rotor bearing system. The stiffness and damping of shaft and housing were included in the model, while the forcing function modeled in Ref. [10] was used for defect induced structural excitation. Patel et al. [17] built a 3-DOF model of bearing with single and multiple point defects on inner

and outer races, while incorporating the masses of races and that of balls. Shah and Patel [18] presented a dynamic model considering the effect of lubricant film, in addition to the effect of masses of the shaft, balls, and housing. Patil et al. [19] formulated 2-DOF model both for the bearings with IR and OR defects, wherein the inclusion of defects in the model was made using additional deflection of balls relative to races, in the form of half sinusoid. Patil et al. [20] incorporated the changes in the lubrication film thickness and load zone span, with shaft rotation due to continuous motion of the balls relative to the load line.

Peterson et al. [21] investigated the effect of circumferential defect on the load distribution and the effective stiffness of a ball bearing. The effects of defect circumferential length, defect depth and raceway surface roughness were studied under static radial and axial loads. The study showed that the stiffness variation is more rapid in case of defective bearing due to repetitive entry and exit of rolling elements into and out of the defect, respectively. Further, the phenomenon of varying stiffness excitation of rigid body modes was also revealed which occurs due to these entry-exit events.

In majority of the work, the rotor and the housing were considered rigid, while in Ref. [22], these were considered deformable. The slice and integral methods were employed to find the overall stiffness at the deformable interface between the outer raceway and housing. According to their results, the smaller housing height has a large influence on the interface stiffness.

In the dynamic models [8,23–25] of ball bearings with localized surface defects, three-dimensional motions of balls along with slip at ball raceway contacts were considered. Since at high speed operations, the dynamic response is strongly determined by centrifugal forces, gyroscopic and spin effects, and slip at ball-raceway contacts, Niu et al. [8] proposed a model for high-speed ball bearings with localized defects on raceways, considering these effects. This work was further extended to bearings with ball defects in Ref. [24] and roller defect in Ref. [25], while accounting for three-dimensional motion of rolling elements.

In most of the earlier models [10,11,13,19], the contact deformation at ball raceway contact is described by a single function, which cannot equally describe all potential localized defect types. Hence, a piecewise response function was proposed, including both time-varying and time-invariant dynamic characteristics as the ball passes over the defect in ball bearing [26–28] and cylindrical roller bearing [29]. Moreover, unlike previous models, these models also took into account the contact deformation at the defect edges. The time varying deflection was represented as half sinusoid while the time invariant deflection was modeled using rectangular function. The impulse force due to local defect was calculated from the ratio of the ball size to the defect length, and the ratio of the length to the width of the defect contact deformation at the defect edge.

Wang et al. [30] used multibody dynamics to compute traction forces, relative slippage, gravity forces, centrifugal forces and gyroscopic moments. These parameters were used to investigate the behavior of cylindrical roller bearing with localized defect on inner and outer races. In [31], Yuan et al. employed multibody kinematics to model the vibration transmission path of bearing rotor assembly and investigated the system response under the presence of simple and compound faults. Recently, Kang et al. [32] have proposed a model that can simulate the bearing operational condition more realistically. Their model incorporates the effect of skidding of rolling element, ball-cage and cage-race interaction, and damping and elasto-hydrodynamic lubrication (EHL). Qin et al. [33] modeled the ball-cage interface as spring damper system and analyzed the impact of local defect on the motion of cage. Beside these, Liu et al. [34] additionally incorporated relative motion of the balls and raceways in their model, to accurately simulate the resulting noise at high speeds.

There are other research works that attempted to explore the dynamic behavior of defective bearing using finite element method [9, 35,36] and bond graph method [37]. Cao et al. [38] integrated analytical formulations with finite element method to model the vibration behaviour of machine tool spindle containing defective bearing. Gazizulin et al. [39] proposed a computationally efficient approach by combining dynamic modeling with finite element method to simulate the fault evolution process due to the repetitive impact of rolling element at the trailing edge.

It is reported in Ref. [40] that the entry and exit events of ball are more clearly revealed in force time plot compared to acceleration waveform, without the aid of signal processing algorithms, and hence the phenomenon of ball passing the defect was modeled in terms of multi-event excitation forces for bearing with OR [41] and IR [40] faults.

It is found from the literature that in defect induced impulse series, the entry is a low frequency event whereas the exit produces impulse in wide frequency range, and it is considered a high frequency phenomenon. Many researchers [7–9,42–45] rely on this dual-impulse theory for estimating the fault size from the duration between the consecutive pulses in the signal, nevertheless, such interpretation might be misguided due to varying compliance vibration which may also yield comparative strength of additional impulses.

In all the previous models reported in literature, the quantitative analysis of the varying compliance vibrations and its strength relative to the defect induced vibration at the incipient stage is missing. It was established from the numerical computation of M. F. While [46] that the changes in deflection and stiffness (or varying compliance) due to orbital motion of cage (leading to change in the position and the number of balls in the load zone) is less than half a percent, and for this reason such inclusions have been ignored from the later models [4][16]. However, it has been established in this work both through numerical analysis and experimental results that the strength of peaks arising at outer race defect frequencies in the frequency spectrum of healthy bearing have nearly comparable magnitude to those appearing because of the smaller sized defects. It has been illustrated further that how the existence of these impulses can considerably alter the characteristics of the impulse arising actually due to the OR defect, both in the signal waveform and the spectrum. As a consequence, the direct estimation of defect size directly on the ground of dual impulse concept is still questionable for systems under general operational condition and the fault diagnosis based on such philosophy lacks reasonable certainty. In the present work, a detailed analysis has been conducted by combining the concepts of impulse force and additional deflection models with suitable alterations, for close prediction of the events occurring at the curved edges of the faults in ball bearing with single OR defect. It is also evident from the existing literature that the sinking depth/ additional deflection in earlier models [7,14,17,19,26–29, 33,47] was determined using a few standard mathematical functions, that is supposed to describe the path followed by the ball while

passing through the defect zone, irrespective of the actual defect profile. However, such predefined path profiles, which are obtained using geometrical relationships of the bearing and the localized defect, are not exactly traced by the ball in real scenarios, but it is also governed by the localized deflection and the bearing kinematics. In view of this, the present work attempts to propose more accurate expressions for time varying localized deflection and ball kinematics, considering all the critical factors guiding the ball travel through the defect.

The overall ball bearing circumference was divided into discrete zones as loaded, unloaded, defect, defect-free zones. The time varying contact stiffness, Hertzian deflection, and contact forces were analytically computed from different relationships, separately applicable to each zone. The time varying elasto-hydrodynamic damping due to squeezing of the oil film at the entry zone of the rotating balls was also considered in the model. Moreover, unlike previous models, where the impulse force was modeled by directly applying impulse train function of defect frequency, a more realistic approach was used in the present work, in which the impulse force was computed from the impact dynamics of the ball, hitting the exit edge of the defect. In addition to this, the incorporation of the dynamic natures of contact forces, load zone, lubricating film thickness, damping, contact stiffness, and their derived parameters due to the continuous motion of the ball-cage assembly, relative to the load line, adds to the accuracy of the proposed model. Finally, the vibration response at the housing of the bearing was obtained from the equations of motion of simplified 2-DOF model of rotor-bearing system adapted from Ref. [41]. The mathematical computation was carried out in a customized solver developed in MATLAB 2019 environment. The generation of defect induced impulses in the vibration waveform both in case of healthy and defective bearings was studied under different speeds and load conditions, and the results are presented in this work. The effect of defect size on the strength of the defect frequency and its harmonics is also shown. The simulated results obtained for different defect sizes show a good correlation with experimental values. The present analysis lays a foundation for future research needs towards accurate bearing fault diagnosis.

The rest of this paper has been organized as follows: Section 2 presents the dynamic modeling and analytical formulations for relevant kinematic parameters, time varying contact stiffness, force, deflection, and the expressions for system's equation of motion. Section 3 shows the simulation results obtained using the proposed dynamic model under different load and speed conditions and the detailed analyses related thereto. Section 4 contains the description of the experimental setup and the experimental results for validation of the simulated response. Finally, Section 5 concludes the paper, highlighting the main findings of the present work, its limitation and the potential future scopes.

2. Dynamic modeling

2.1. Possible ways through which the ball circumnavigates the defect

The vibration response of a rotary system with a defective bearing is largely governed by the severity of the defect. For a defect to be localized, its size should be sufficiently small to prevent the rolling element from touching the defect base while making a move from entry to exit edge of the defect. According to Ref. [40], the localized defect can be defined by the entry/leading edge, and the exit/trailing edge. Depending upon the gap between these two edges, the defect depth, and the bearing geometry, the ball can generate following two types of events while traversing the defect:

2.1.1. Single impact event (localized defect)

The single impact event happens when the defect spans over a small area yet having larger depth. This is often the incipient stage of the spall formation. Fig. 1(a) and (b) depict the two cases of localized defects. In Fig. 1(a), the ball hits the exit edge without touching

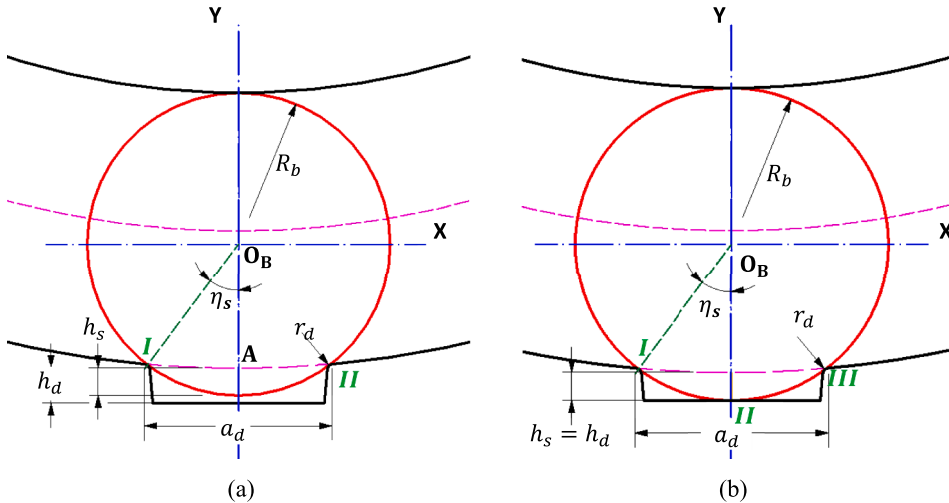


Fig. 1. Ball in contact with OR defect in single-impact (localized defect) case: (a) $h_{s,max} < h_d$; (b) $h_{s,max} = h_d$.

the defect base. Hence, only two events, I-entry event, and II-exit event, can be observed. In both the cases, the impact is observed only once during the ball movement over the defect zone.

With reference to Fig. 1, the angular span (η_s) of the defect about its center, can be expressed as:

$$\eta_s = \sin^{-1} \frac{(a_d/2 + r_d)}{(R_b + r_d)} \quad (1)$$

where a_d and r_d are the defect length and defect edge radius, respectively, and R_b symbolizes the ball radius.

Also, for small defect, arc IA can be considered straight. Hence, the length $O_B A$ can be written as:

$$(R_b) \cos \eta_s = R_b - h_d \quad (2)$$

The ball can sink inside the defect, maximum up to the depth of defect (h_d), i.e.:

$$h_{s,max} = R_b(1 - \cos \eta_s); h_{s,max} = [0, h_d] \quad (3)$$

When $h_{s,max} = h_d$, the ball simultaneously strikes with the defect bottom and the exit edge, as shown in Fig. 1(b). This is a critical case, which is nearly impractical to achieve, and it only represents the transition period during which the defect transforms from localized to extended zone.

2.1.2. Multi-impact event (extended defect)

The continued operation of bearings with localized defect leads to defect propagation, thereby transforming it to extended defect causing a possibility of double or multi-impact case. This encompasses occurrence of impacts at the bottom of the defect in advance to striking of the ball with the exit edge.

The ball first hits the defect base then travels to the exit end either under no contact force or under finite contact force or intermittently under no force and finite force values, depending on the defect depth, defect surface profile and the operating load which will determine the overall deflection and consequently the contact status at different positions. It can be seen from Fig. 2 that the ball sink, h_s diminishes as the ball travels past the defect surface. This generates the possibility that the ball is compressed under load causing the ball to strike with the asperities of rough surface of defect, thereby producing multiple impacts before making its final exit. Although the profile of the rough surface will be exceptionally uncertain and it will vary from case to case, its correct prediction is not necessarily required for fault diagnosis purpose for which the correct time localization of entry and impact events should suffice.

The multi-impact event occurs when the depth of the defect is small than the critical value corresponding to its span, i.e., $h_d < R_b(1 - \cos \eta_s)$. Fig. 3 shows a typical relation between h_d and a_d , wherein the curve representing case (1.b) separates the single impact and the multi-impact zones. The increasing defect span at a fixed value of h_d gives rise to increased chances of multi-impact events.

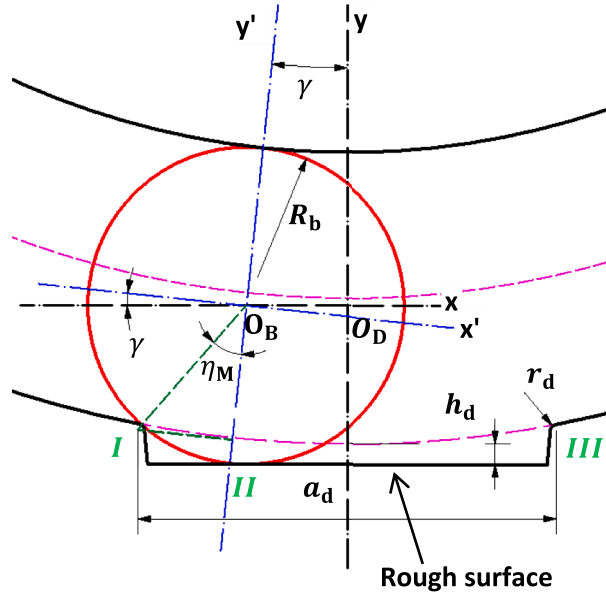


Fig. 2. Ball in contact with OR defect in multi-impact case.

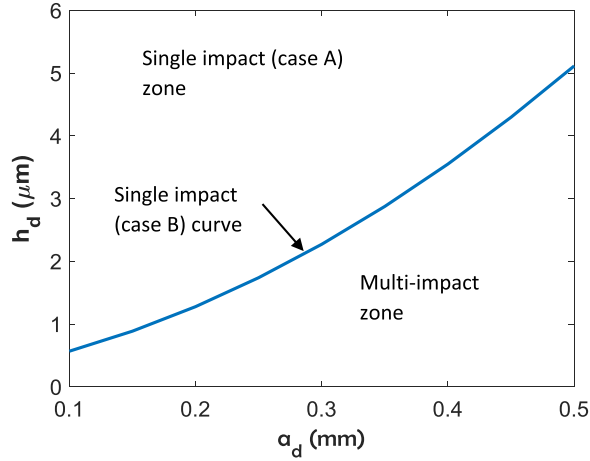


Fig. 3. Plot showing typical relationship between defect span (a_d) and the defect depth (h_d)

2.2. Piecewise force-deflection modeling

For accurate fault diagnosis, it is immensely important that the entry and exit events of fault are precisely located in waveform plot of bearing vibration signal. When the fault is new, the edges are sharp, but as the bearing continues to operate, the edges get plastically deformed, thereby forming curvature at entry and exit zones, though, of extremely small radii. Hence the defect edges are considered curved in the proposed vibration model of ball bearing with localized OR defect. The assumptions taken for modeling the response of

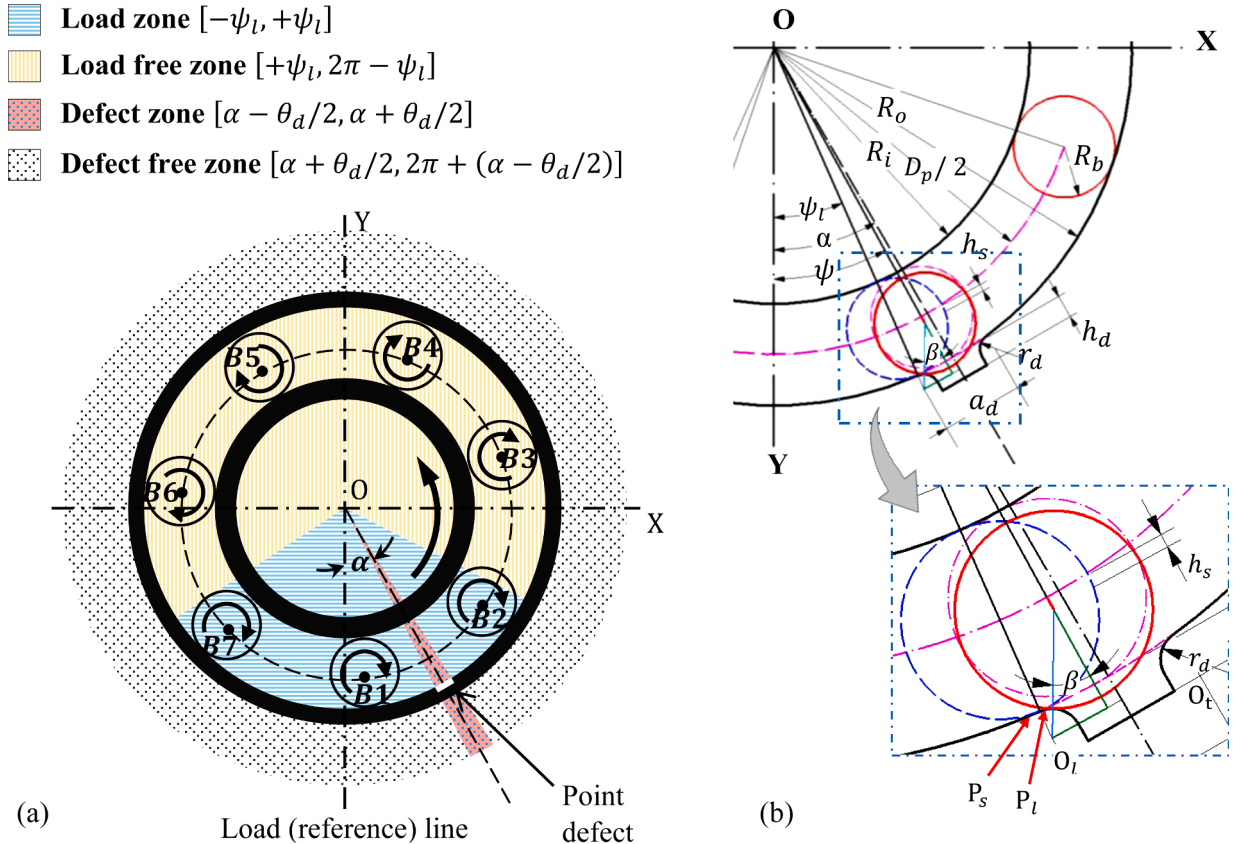


Fig. 4. (a) Schematic of ball bearing with OR defect, (b) Bearing geometry with OR defect.

deep groove ball bearing having the aforementioned OR defect, are listed below:

- 1 The outer ring is stationary, while the inner ring rotates with the shaft.
- 2 The inner ring is firmly mounted on the shaft while the outer ring inside the housing, and there is no relative motion between the inner ring and the shaft, and similarly between the outer ring and the housing.
- 3 Elasto-hydrodynamic film lubrication exists at ball-raceway contacts.
- 4 Except the contact zone, rest of the bearing components behave as stiff elements. The contact deformation is elastic but non-linear, as per Hertzian deformation theory.
- 5 The applied load is purely radial and static, and the thermal effect is not considered.
- 6 The defect is localized, and it is present on the outer race. The defect is located in the load zone because outside the load zone, the ball will lose contact with the races and the defect will have only little influence on the vibration signal.
- 7 The defect edge is curved and has some finite radius of curvature.
- 8 The defect is symmetric about its center, and therefore, the shape of the defect edges at entry and exit are identical.
- 9 The angular span of the defect (i.e. the size) is calculated with respect to the location of the centers of curvature of defect edges at entry and exit.
- 10 Change in outer race groove radius due to occurrence of spall is non-considerable.
- 11 The ball-cage interaction and the effect of clearance between the cage and the balls are ignored.
- 12 The mass of the ball is negligibly small.
- 13 Bearing operates at moderate speed at which the effect of centrifugal force of the balls is small.
- 14 The ball performs pure rolling without slip.

Fig. 4(a) and **(b)**, respectively depict the schematic of a typical ball bearing with a point defect on the outer race, in XY coordinate frame, and all the important geometrical parameters that will be used in deriving the dynamic response behavior of the system. Point O represents the center of the bearing under no load. The load line is taken as the reference to define the angular location of the cage and the balls at any instant. The defect is located at an angular location α from the load line. The shaft is rotating in counterclockwise direction, thereby setting each ball in clockwise rotational motion. The complete bearing has been circumferentially divided into four zones, namely load zone, load free zone, defect zone, and defect-free zone. The respective ranges of all the zones are also given alongside the bearing schematic. The time varying characteristics will be determined analytically from different relationships, separately applicable to each sliced zone.

As seen from the enlarged view of **Fig. 4(b)**, point P_s marks the entry of the ball in the defect region. This is an inflection point where the curvature at raceway contact changes from concave ($-R_o$) to convex (r_d). After this point, the ball will begin sinking into the defect region. The point P_l represents an arbitrary location of the ball raceway contact at the defect entry zone. On further rotation, the sinking depth (h_s) of the ball inside the defect will increase till it reaches a maximum value at the center of the defect, and thereafter, it will decrease again and will attain zero value at the exit of the defect zone. The time varying value of h_s determines the overall magnitude of contact deflection and the resulting stiffness force, hence, the correct expression of variable ball sink is important for accurate modeling of the dynamic response of defective ball bearings. As already stated in [Section 1](#) that majority of the earlier research work [7,14,17,19,26–29,33,47] utilized standard profiles for expressing sinking depth/ additional deflection of the balls

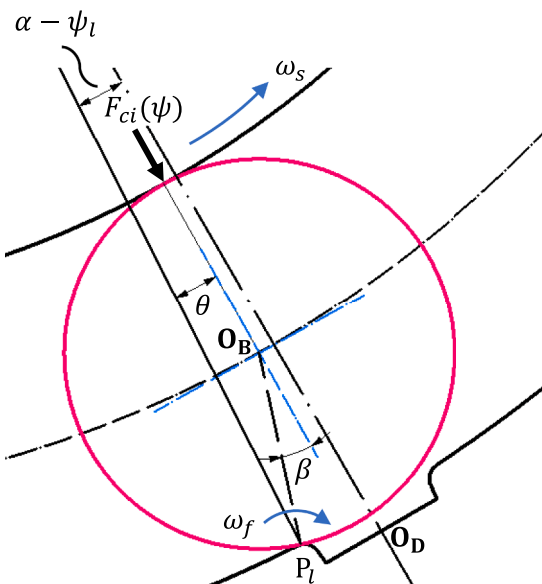


Fig. 5. Kinetics of a ball traversing an OR defect in a ball bearing.

passing the defect, such predefined profiles do not simulate the real scenario, where the actual path traced by the ball is also governed by the localized deflection and bearing kinematics under a given combination of speed and load. Considering this, the present work attempts to propose a new expression of time varying sinking depth for localized defects with round edge profiles considering all the critical factors guiding the ball across the defect.

In general, the major events that are encountered by a ball between the entry and exit events of a localized defect can be listed as follow:

- 1 Ball roll over the entry (leading) edge.
- 2 Ball hit at the exit (trailing) edge, causing an impact.
- 3 Ball bounce and return to the OR track, quickly after impact.

The kinematics of the ball at the abovementioned events can be derived as follow:

2.2.1. Angular velocity (ω_f) of the ball about the leading edge just before hitting the trailing edge

Referring to Fig. 5, the equation of motion obtained by balancing the moment due to the ball turning around the leading edge about an instantaneous point P_l , while ignoring the negligible force and moment due to mass of the ball, takes the following form:

$$\begin{aligned} J \frac{d\omega}{dt} &= F_{co}R_b \sin\beta = F_{co}R_o \sin\theta; \text{ where, } \theta = \psi - \psi_l \\ 0 \leq \beta &\leq \eta; \text{ and } 0 \leq \theta \leq \frac{\theta_d}{2} \text{ for } \psi_l \leq \psi \leq \psi_t \end{aligned} \quad (4)$$

where $\omega = \frac{d\theta}{dt}$, and $\frac{d\omega}{dt} = \frac{d^2\theta}{dt^2}$; F_{ci} and F_{co} are the contact forces at the ball-IR and the ball-OR contacts, respectively. β is the instantaneous angular location of ball-OR contact with respect to ball center, O_B while θ is measured from bearing center, O. Moreover, θ_d and η represent the angular span of the defect about the bearing center and the ball center, respectively.

For small value of θ ; $\sin\theta \sim \theta$, thus Eq. (4) becomes:

$$\frac{d^2\theta}{dt^2} = \frac{F_{co}R_o}{J} \theta \quad (5)$$

Taking arbitrary variable, $rf = \frac{F_{co}R_o}{J}$, and considering that the contact force, F_{co} at outer raceway (and hence the term rf) will stay nearly constant for the period during which the ball rolls over the leading edge, Eq. (5) can be written as:

$$\frac{d}{dt} \left[\left(\frac{d\theta}{dt} \right)^2 - rf \theta^2 \right] = 0 \quad (6)$$

Integrating Eq. (6) with respect to time 't' yields:

$$\left(\frac{d\theta}{dt} \right)^2 - rf \theta^2 + C_1 = 0 \quad (7)$$

Since at $\theta = 0$, $\frac{d\theta}{dt} = \omega_b$; the constant $C_1 = -\omega_b^2$, where ω_b denotes the ball angular velocity outside the defect zone. Thus, the angular velocity expression of the ball located at an angle θ is given by:

$$\omega^2 = \omega_b^2 + rf \theta^2 \quad (8)$$

As the ball reaches the center of the defect, it is on the verge of hitting the trailing edge. At this instant, the expression of angular velocity (ω_f) becomes:

$$\omega_f^2 = \omega_b^2 + rf \left(\frac{\theta_d}{2} \right)^2 \quad (9)$$

2.2.2. Velocity (\dot{x}) of the ball after hitting the trailing edge

The equation of motion at the instant the ball hits the trailing edge is given by:

$$\frac{7}{5}m_b \ddot{x} + k_c x^{3/2} = F_{co} \cos\eta \quad (10)$$

On integration, Eq. (10) takes the following form:

$$\frac{\dot{x}^2}{2} + \frac{2k_c}{7m_b} x^{5/2} - \left(\frac{5F_{co}}{7m_b} \cos\eta \right) x + C = 0 \quad (11)$$

Now since $x(0) = 0$ and $\dot{x}(0) = v_0$; $C = -v_0^2/2$; where v_0 is the linear velocity of the ball along the direction of the impact, and it is given by:

$$v_0 = v_{\text{net}} \cos\left(\theta_{\text{net}} + \frac{\pi}{2} - 2\eta\right) \quad (12)$$

v_{net} is the net velocity of the ball which is a vector sum of the velocity ($v_1 = \omega_f R_b$) along the direction of impulse and the velocity ($v_2 = \omega_c D_p / 2$) due to cage rotation, both acting at an angle η from each other, as illustrated in Fig. 6.

$$v_{\text{net}}^2 = v_1^2 + v_2^2 + 2v_1 v_2 \cos\eta \quad (13)$$

and θ_{net} is the angle made by v_{net} with respect to v_1 .

$$\tan\theta_{\text{net}} = \frac{v_2 \sin\eta}{v_1 + v_2 \cos\eta} \quad (14)$$

The final expression for the linear velocity of the ball is thus given by Eq. (15):

$$\dot{x}^2 = v_0^2 + \left(\frac{10F_{co}}{7m_b} \cos\eta \right) x - \frac{4k_c}{7m_b} x^{5/2} \quad (15)$$

The maximum compression ($x_{c,\text{max}}$) due to the impulse can be obtained numerically using Eq. (15) after putting $\dot{x} = 0$, i.e.

$$0 = v_0^2 + \left(\frac{10F_{co}}{7m_b} \cos\eta \right) x_{c,\text{max}} - \frac{4k_c}{7m_b} (x_{c,\text{max}})^{5/2} \quad (16)$$

2.2.3. Piecewise stiffness, force and deflection

The contact force due to stiffness of ball-raceway contact is given by Hertzian non-linear equation, Eq. (17) [48]:

$$F(\psi) = K_n [\delta(\psi)]^{3/2} \quad (17)$$

where the load deflection constant (K_n) is a function of bearing geometry and material only, and it is independent of angular location. It can be calculated using Eq. (18) [49]:

$$K_n = \pi \kappa E' \sqrt{\frac{2\epsilon R}{9F^3}} \quad (18)$$

where κ is the ellipticity parameter of contact ellipse, E' is the effective elastic modulus of contact, ϵ and F are the complete elliptic integral of first and second kind, respectively, and R is the effective radius of curvature. Since the contacting geometry changes due to arrival of defect, the value of K_n is also affected and hence it will be different for defect free and defective zones. Moreover, the value of K_n will be different at entry and exit points (where the curvature becomes zero) from the value corresponding to ball inside the defect (where the defective surface has the curvature of radius equal to defect edge radius). Further, as per our numerical computations over a similar range of bearing with typical OR point spalls, this change is only within 5% at inflection point.

The contact stiffness (K_{cy}) can be expressed in terms of load deflection constant and the contact force at angle ψ , as follow:

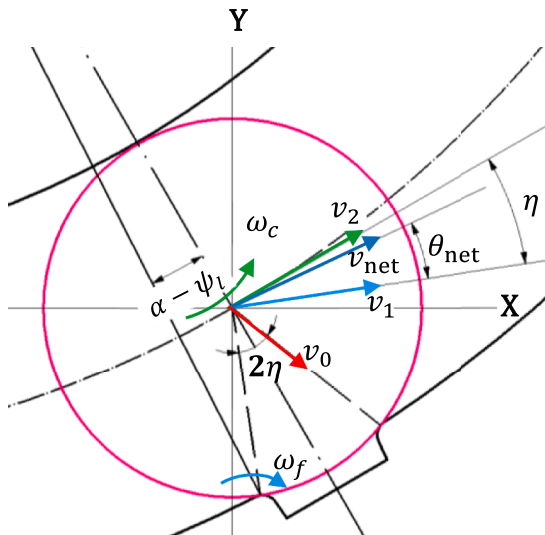


Fig. 6. Kinematics of the ball traversing an OR defect in a ball bearing.

$$K_{c\psi} = \frac{3}{2} K_n^{2/3} F_\psi^{1/3} \quad (19)$$

The total deformation, $\delta(\psi)$ at the ball-race contact can be expressed as:

$$\delta(\psi) = x \cos \psi - \left(\frac{p_d}{2} + h_s \right) \quad (20)$$

where x represents the overall displacement of inner ring relative to the outer ring, p_d is the diametral clearance, and h_s denotes the ball sink/ additional deflection occurring only inside the defect zone.

Moreover, if the bearing is lubricated, then the minimum film thickness, h_{\min} of oil film must also be included in the total deformation relationship:

$$\delta(\psi) = x \cos \psi - \left(\frac{p_d}{2} + h_s + h_{\min} \right) \quad (21)$$

For static equilibrium of the ball bearing in the direction of the applied load, it is necessary that the radially applied load be balanced by the total contact forces due to each ball in the load zone, i.e.,

$$F_r = K_n \sum_{\psi=-\psi_{LZ}}^{+\psi_{LZ}} \left[x \cos \psi - \left(\frac{p_d}{2} + h_s + h_{\min} \right) \right]^{3/2} \cos \psi \quad (22)$$

where $\psi_{LZ} = \cos^{-1}(p_d / 2x)$, and the range $[-\psi_{LZ}, +\psi_{LZ}]$ defines the extent of the load zone. Only the balls located inside this range will make contact with both the races and transmit the load between the shaft and the housing. Since both the deflections and the angular range of the load zone are functions of applied radial load, their values are obtained by iteratively solving Eq. (22), for which Newton's bisection method was applied in the present work.

2.2.4. Ball sink (h_s)

It can be derived from Case A of Section 2.1.1 that:

$$h_s = (1 - \cos \beta)(R_b + r_d) \quad \text{for small } r_d \quad (23)$$

where β can be calculated from the following relation:

$$\sin \beta = \frac{(R_o + r_d)}{(R_b + r_d)} \sin \theta \quad (24)$$

It is established from the previous discussion that:

$$\frac{d^2 \psi}{dt^2} = \frac{F_{ca}(R_o + r_d)}{J} \theta \quad (25)$$

And since $\theta = \psi - \psi_l$, Eq. (25) becomes:

$$\frac{d^2 \theta}{dt^2} = r f \theta \quad (26)$$

The solution of Eq. (26) is given by:

$$\theta(t) = A e^{(r f) t} + B e^{-(r f) t} \quad (27)$$

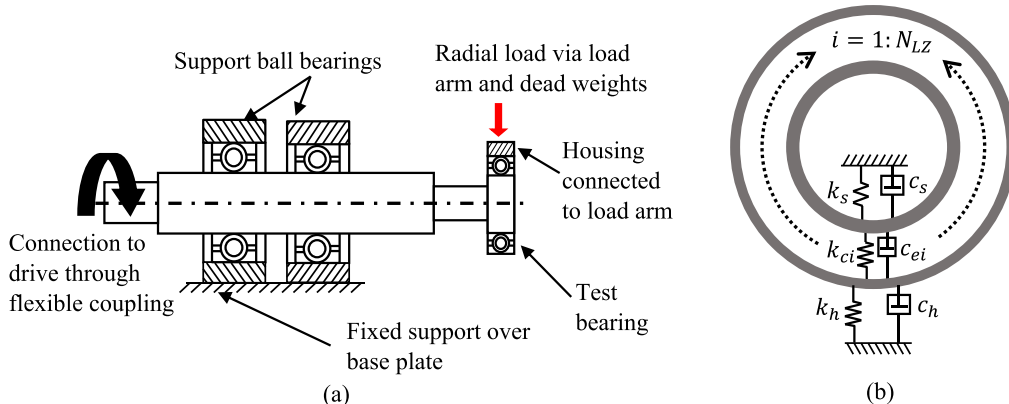


Fig. 7. (a) Schematic of experimental test rig (b) Equivalent lumped parameter vibration model.

The boundary conditions are:

$$\theta(t_l) = 0; \quad \theta(t_{dc}) = \theta_d/2$$

where t_l and t_{dc} denote the time when the ball center is located at defect entry point and at the defect center, respectively.

Using the above boundary conditions, the expressions for arbitrary constants, A and B, become:

$$A = \frac{\theta_d/2}{e^{rf t_{dc}} - e^{rf(2t_l-t_{dc})}}; \quad B = -Ae^{2rf t_l} \quad (28)$$

Hence, the generalized expression for θ as a function of time can be expressed as:

$$\theta(t) = \frac{\theta_d}{2} \left[\frac{e^{rf t} - e^{rf(2t_l-t)}}{e^{rf t_{dc}} - e^{rf(2t_l-t_{dc})}} \right] \quad (29)$$

2.2.5. Equations of motion

The schematic and the equivalent lumped parameter vibration model of the test setup have been shown in Fig. 7. The support bearing contains two deep groove ball bearings in tandem at small gap, as a result of which this end of the shaft, which is connected to motor through flexible coupling, is considered rigid. The 2-DOF model reported in this work has been adapted from Ref. [41] with modified expression for impact velocity, force at the exit edge of the defect, and time varying ball sink, and inclusion of EHL damping at the ball-raceway contact.

The equations of motion for the vibration model depicted in Fig. 7(b) will be given as:

$$m_s \ddot{x}_s + (c_s + c_e) \dot{x}_s - c_e \dot{x}_h + k_s x_s + \sum_{i=1}^Z \mu_i K_{ni} (x_s - x_h) \cos \psi_i = 0 \quad (30)$$

$$m_h \ddot{x}_h - c_e \dot{x}_s + (c_e + c_h) \dot{x}_h + k_h x_h - \sum_{i=1}^Z \mu_i K_{ni} (x_s - x_h) \cos \psi_i = F_{\text{imp}} - F_r$$

where $\mu_i = \begin{cases} 1; & \text{for } i^{\text{th}} \text{ ball in load zone} \\ 0; & \text{for } i^{\text{th}} \text{ ball outside load zone} \end{cases}$; m_s represents the equivalent mass of the shaft and the inner race acting at the center of the bearing, m_h is the mass of the housing and the outer race.

c_s and c_h are the material damping of shaft and housing, respectively. The method presented in Ref. [40] was applied for finding the values of material damping of shaft and housing, according to which the following relationship holds:

$$c_{s,h} = LF \times k_{s,h} / \omega_{\text{ex}} \quad (31)$$

where LF is the loss factor, which is a material property, and ω_{ex} is the excitation frequency.

The term c_e in Eq. (30) represents squeezed film damping, acting at the entry of each ball raceway contact. The following relationship, which was derived by Hagiud and Gafitanu [50] using Reynold's lubrication equations, was employed to calculate the value of c_e :

$$c_e = \frac{3\pi}{\sqrt{2}} \left(\frac{R_x}{h_{\min}} \right)^{1.5} \eta_0 (2a) \quad (32)$$

where R_x represents the effective radius of curvature in the rolling direction of ball, a represents the semimajor axis of the elliptical contact area, and η_0 is the oil dynamic viscosity at atmospheric condition.

The expressions for R_x and a are well established and can be found in Ref. [49]. Further detail on computation of c_e and its dependence on different geometrical parameters of bearing under a range of applied radial load can be found in literature [51].

Following the methods used in Ref. [17], the stiffness (k_s) of the shaft was calculated using area-moment method, whereas the stiffness (k_h) of the housing was determined from finite element analysis using ANSYS-14.

In Eq. (32), h_{\min} represents the minimum thickness of oil film under compression inside the contact patch. The mathematical relationship for minimum film thickness has been provided by various authors [52–55], and the expression given by Hamrock and Dowson [49,55] has been adopted in this work, which is given by Eq. (33).

$$H_{\min} = \frac{3.63U^{0.68}G^{0.49}(1 - e^{-0.68k})}{W^{0.073}} \quad (33)$$

where H_{\min} ($= h_{\min}/R_x$) is the dimensionless film thickness, U ($= \eta_0 u_x / E' R_x$) is the dimensionless speed parameter, G ($= \xi E'$) is the dimensionless material parameter and W ($= F_y / E' R_x^2$) is the dimensionless load parameter.

Damping at lubricated contacts may also arise from frictional losses due to balls moving relative to races, however, due to lubrication the frictional effect will be extremely small, and hence the frictional damping is not accounted in the proposed model.

The value of impulse force (F_{imp}) due to striking of ball with the exit edge of the defect on outer race can be determined by

calculating the contact force on that edge at the end of compression due to impact, i.e. $F_{\text{imp}} = K_n x_{c,\text{max}}^{1.5}$. The value of maximum compression ($x_{c,\text{max}}$) at the end of the impact can be obtained numerically from Eq. (16).

3. Numerical simulation

A dedicated solver was designed on MATLAB 2019a platform that takes in different operating conditions as per the user requirements and provides the corresponding vibrational characteristic and kinematic parameters, based on the expressions given in

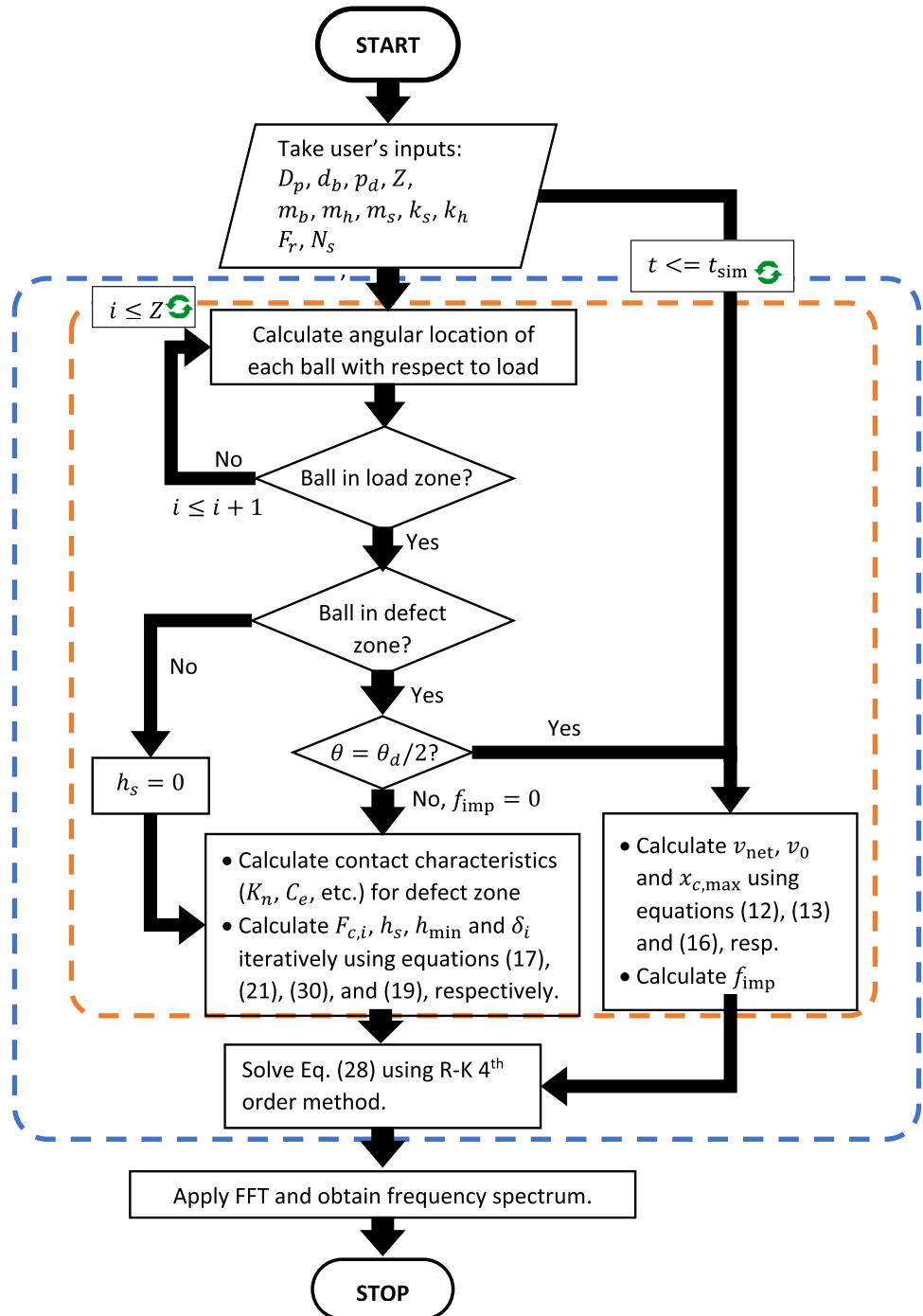


Fig. 8. Algorithm for numerical simulation.

Section 2.2. The algorithm working behind the solver is depicted in Fig. 8. To start the algorithm, the input is fed to the solver in the form of bearing and defect geometry, operating conditions, mass and stiffness characteristics of shaft and housing. At a particular time, the angular location of each ball is determined, and the location of each ball is identified with respect to the four zones: loaded, unloaded, defect and defect free zones. The angular range of the load zone, number of balls in the load zone and contact deflection were calculated numerically by solving Eq. (22) using Newton's bisection method. For balls in the load zone, the contact characteristics (ball sink, overall deflection, film thickness, contact stiffness, squeezed film damping, etc.) are evaluated based on the defect and defect-free regions. While these calculations are skipped for the balls residing outside the load zone because these balls will not contribute to the contact parameters. For balls in the defect zone, impulse force is zero only except when it reaches the defect center and hits the exit edge (i.e. $\theta = \theta_d/2$). At this point, the ball rolling velocity about the leading edge, cage velocity, and the ball velocity along the direction of impact are determined, based on which the maximum compression during the impact and the resulting impact force are next calculated. The acceleration responses ($\ddot{x}_{s,h}$) of shaft and housing are obtained by solving equations of motion, given in Eq. (30), using fourth order Runge Kutta method. These computations are repeated with time step (Δt) of 5e-7 s, until the simulation time (t_{sim}) set by the user is reached.

The extremely small timestep chosen in the present work aims at capturing confidently every critical event in the waveform signal during which the ball negotiates the small sized fault, especially at the entry and impact phenomena. The solver returns the output in the form of the orbital location of the cage, number of balls residing in the load zone, elliptical contact parameters, effective oil film damping, impulse force resulting from the impact of the ball with the exit edge of the defect, and the vibration response (displacement, velocity, acceleration). Besides, other intermediate parameters including EHL parameters, defect frequency, Hertzian contact parameters (related to contact geometry, stiffness and damping), etc., which are utilized in the calculation of vibration response, are also displayed by the solver.

The relevant bearing specifications and the other important parameters of the rotor bearing assembly, used in the present analyses, are listed in Table 1.

3.1. Healthy bearing response

When a static radial load is applied on the bearing, it gets distributed to the balls lying in the load zone. The amount of load carried by each ball depends on its location with respect to the load line, and hence as the bearing rotates, the load distribution changes. This also causes the load zone span to change, which can be determined using either summation (Stribeck's) [46] or integral methods [48].

At the start of the simulation ($t = 0$ s), the first ball (B1) is supposed to lie on the load line, as shown by configuration A in Fig. 9(a). The center O_{B1} of ball 1 is taken as the reference point on the cage, and thus the location of ball 1 will define the rotation of the cage with respect to the load (or reference) line. With the rotation (ω_s) of shaft, the cage will turn by angle ψ so that ball 1 will move towards the initial location of ball 2, whereas ball 7 will approach the load line. On rotation of the cage by angular spacing of the ball (i.e. when $\psi = \phi_s$), ball 7 will reach the load line, and similarly, all the other balls will take the preceding positions of the balls next to them. At this point of time, the arrangement of the balls will become similar to that as previous (i.e. configuration A). Fig. 9 depicts how the angular span (ψ_{LZ}) of the load zone changes with the rotation (ψ) of the cage (and change in the balls' configuration).

Fig. 10(a) describes the angular motion of the ball, located on the load line, by angle ϕ_s , thereby giving way to the preceding ball to reach the load line. On completion of one full rotation of the cage, the first ball returns back to the load line, and all the other balls will take their previous locations as shown in Configuration A. Since after every rotation of angle ϕ_s , the ball arrangement is repeated, the dynamic characteristics of the bearing will be periodic at the angular spacing (ϕ_s) of the ball. The variation in the number of load

Table 1
Bearing parameters.

Bearing type	SKF BB1B420204
Pitch diameter, D_p (mm)	32.94
Ball diameter, d_b (mm)	8.7
Diametral clearance, p_d (μm)	10
Number of balls, Z	7
Angular spacing between balls, ϕ_s (deg)	51.42
OR fault frequency ratio, $\omega_o = f_{\text{OR}}/f_s$	2.576
Mass of ball, m_b (kg)	0.0027
Mass of OR and housing, m_h (kg)	0.445+0.890
Mass of IR and overhung shaft, m_s (kg)	0.210+0.165
Housing stiffness, k_h (N m^{-1})	1.451e+10
Shaft stiffness, k_s (N m^{-1})	4.667e+8
Housing damping, c_h (N s m^{-1})	769.78
Shaft damping, c_s (N s m^{-1})	24.76
Applied radial load, F_r (N)	100
Shaft speed, N_s (rpm)	1500
BPFO (theoretical) at $N_s = 1500$ rpm	64.38

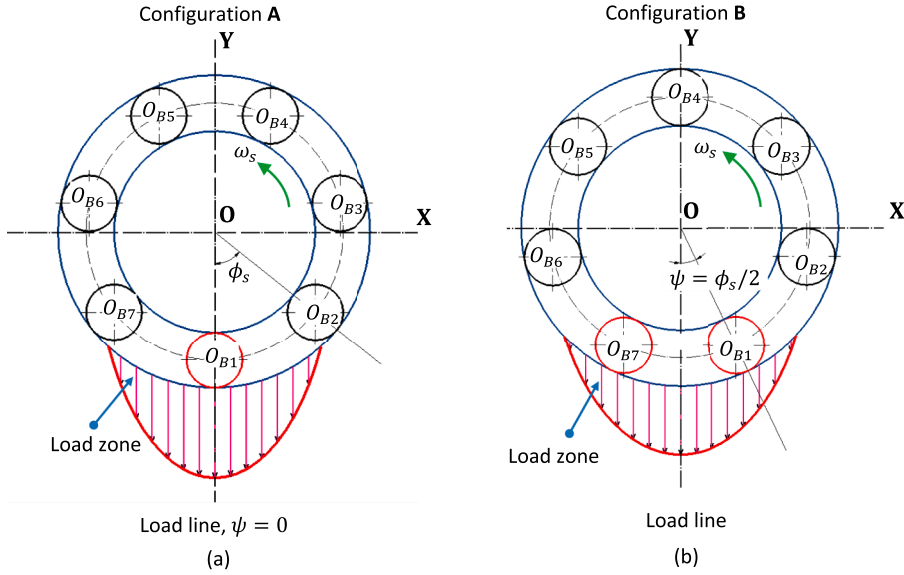


Fig. 9. Effect of cage orientation on the angular span of load zone.

bearing balls (N_{LZ}), due to continuous change in the load zone span with time, is depicted in Fig. 10(b) for a deep groove ball bearing under the application of 100 N of radial load and 1500 rpm of shaft speed. Fig. 10(c) shows the snippet of this variation in N_{LZ} with cage rotation for one period i.e. $\psi [0, \phi_s]$.

As depicted in Fig. 10(c), when the first ball moves from $\psi = 0$ rad (at $t = 0$ s) to $\psi = 0.29638$ rad ($\approx 17^\circ$), the load zone extends and the number of balls in the load zone (N_{LZ}) increases from one to two (i.e. ball 7 enters the load zone). This increase in the number of balls (N_{LZ}) occurs only momentarily, and exists only for the duration in which a ball departs from the load region and a new ball enters the load zone. Ball 1 resides in the load zone along with ball 7 until the cage is rotated by about 0.6 rad ($\approx 34^\circ$), where ball 1 exits and only seventh ball now takes up the overall load. This occurs until ball 7 reaches the load line ($t = 0.01553$ s), whereby the cage rotates by ϕ_s ($= 0.897$ rad or 51.43°). This process is repeated in a similar manner between ball 7 and ball 6 until the cage makes another rotation, and the same cycle keeps repeating as the shaft continues to rotate.

It is inferential from N_{LZ} and ψ curves of Fig. 10(c) that the new ball enters before the older ball exits. These events (decreasing or increasing in N_{LZ}) cause load redistribution between the participating balls, generating a first impulse due to entry of a new ball in the load zone, and a second impulse due to exit of an older ball from the load zone. These impulses are manifested in the acceleration response of the housing (\ddot{x}_h) as shown in Fig. 11, which repeat at OR frequency ($f_{OR} \approx 64.4$ Hz), as the cage takes $1/f_{OR}$ (i.e. 0.01553 s) time to lapse ϕ_s angle of rotation.

A detailed analysis of the effect on the acceleration response of the bearing due to different loads and speeds are provided in the next subsections.

3.1.1. Effect of F_r on healthy bearing response at $N_s=1500$ rpm

Since the span of the load zone changes with applied radial load, it is important to study the influence of the load on the impulses produced by the load redistribution phenomena. Fig. 12 shows the acceleration response at the housing (\ddot{x}_h) of the healthy ball bearing under three different values of load, as $F_r = 100$ N, 500 N and 1000 N.

The following effects can be observed with changing radial load:

- 1 The impulses become stronger at higher values of load, because at higher loads, the impulse force F_{imp} , which is indirectly a function of contact force, is large.
- 2 The impulses due to change in the values of N_{LZ} are distinctly visible at $F_r=100$ N and $F_r=500$ N, while the two impulses superpose at $F_r=1000$ N. At both $F_r=100$ N and $F_r=500$ N, the impulse is stronger when N_{LZ} rises, compared to when it decreases. This is because, when the number of balls are increased, the amount of load on each ball is reduced, due to which the individual damping coefficients due to each contact is also reduced, thereby resulting in high spikes. Contrary to this, when lesser number of balls lie in the load zone, the amount of load is high at each contributing ball, and the resultant damping is more, and therefore the impulse is weaker.
- 3 The separations between the two impulses vary with change in the load. At 500 N radial load the two impulses are distinctly visible, however at 1000 N load, the second event (due to exit of the ball from the load zone) sets forth before the impulse due to the first event (due to entry of the ball in the load zone) is considerably damped out. Similar trends will be observed for different values of loads, however, N_{LZ} will switch between other steps in that case. The span between first and second impulses will again depend on the value of radial load.

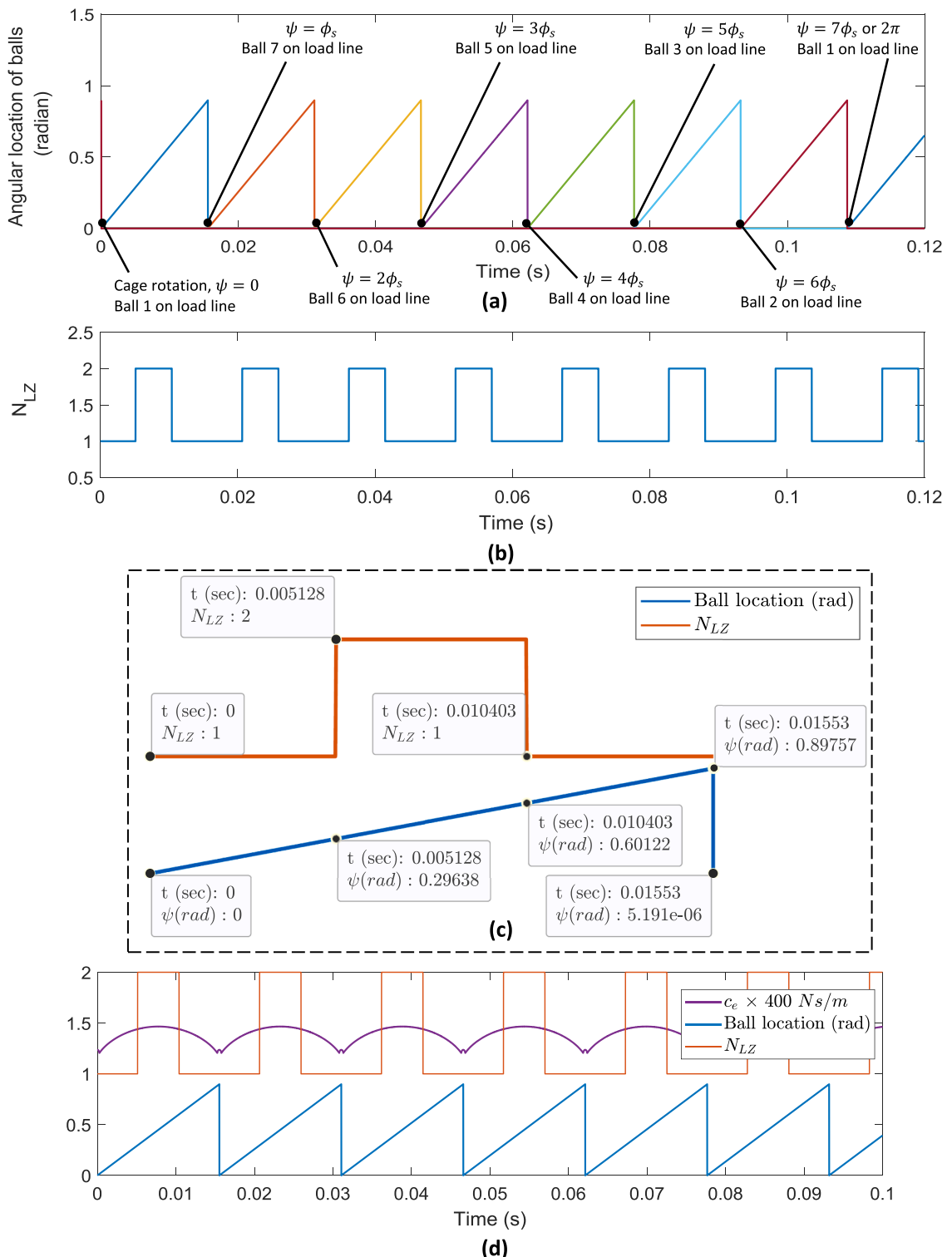


Fig. 10. Change in the bearing configuration with shaft rotation (a) angular location of balls, (b) number of balls in the load zone, (c) zoomed view of (b), and (d) squeezed film damping.

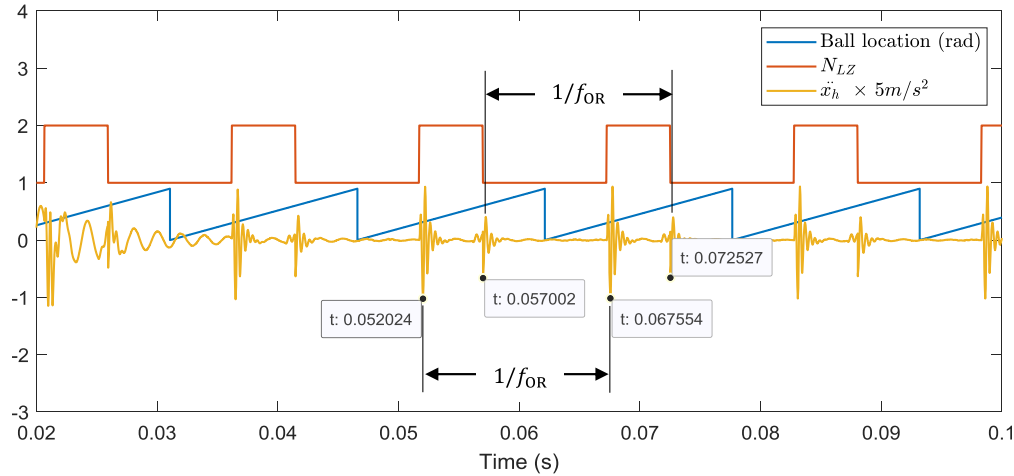


Fig. 11. OR response of healthy bearing at $N_s=1500$ rpm and $F_r=100$ N.

3.1.2. Effect of N_s on healthy bearing response at $F_r = 1000$ N

Beside load, the response of the bearing is also a function of bearing speed which determines the frequency of occurrence of impulses. The effect of speed on healthy bearing response is shown in Fig. 13, from where it is visible that the rotational speed of the shaft has no influence on the acceleration magnitude, however, as expected, the frequencies of impulses vary proportionally with the speed.

Even though the separation between the first and second impulses also varies with the rotational speed, the effect is not as pronounced as that due to load, as observed in Fig. 12. It can be noticed that as the speed increases, the bearing does not find sufficient time for damping of the vibration spikes produced by the first event, and soon the second spike occurs. Hence, at higher values of speed the two spikes merge and form a single impulse. From this and the previous subsection, it can be deduced that the impulses due to exchange of balls in the load zone is a combined function of applied load as well as the rotational speed of the shaft.

3.2. Defective bearing response

When a spall starts emerging on the OR of the bearing, additional spikes are introduced in the response curve, which arise out of impact caused by the striking of the balls with the trailing edge of the point defect. Like varying compliance vibrations, these impulses also repeat at outer race ball pass frequency (BPFO or f_{OR}). To conduct a detailed analysis of the impact phenomenon and estimate the relevant kinematic parameters, the mathematical model proposed in Section 2.2 was solved for the bearing with specifications given in Table 1 and for the defect parameters listed in Table 2.

Fig. 14 shows the kinematics of the ball hitting the trailing edge of the defect. The impact is extremely short lasting (having order of magnitude of '-9' in the present case), as shown in Fig. 14(a) and (b). During the impact, the maximum Hertzian deflection ($x_{c,max}$) at the trailing edge of the defect increases from zero to $7.173 \mu\text{m}$ nearly in no time and stays constant at this value for rest of the impulse duration. On the other hand, the striking velocity of 0.6821 ms^{-1} of the ball dies out to about zero, spontaneously, and remains nearly constant till the end of the impact.

The time varying deflection (h_s) of the ball in the defect region, which has been incorporated in this work, is plotted in Fig. 15(a), from where it can be seen that as the ball approaches the center of the defect, the ball sinks deeper and it finally attains the maximum value, exactly when it reaches the center of the defect. The spike of the impulse force (F_{imp}) due to striking of the ball with the exit edge of the defect is also visible at this location. Moreover, the variations in the value of squeezed film damping of the bearing due to movement of ball inside the defect are depicted in Fig. 15(b).

It can be observed from Fig. 15(b) that when the ball is in the defect zone, the squeezed film damping is drastically reduced. This is due to the reduction in the contact force for the ball residing in the defect zone. As a result of reduced damping, the defect induced vibration persists for a longer duration and the operational performance of the bearing gets deteriorated, which eventually is responsible for shortening of the bearing life.

Fig. 16 to Fig. 18 display the response of the defective bearing with defect parameters listed in Table 2 under three values of load. In all the simulated waveforms, three sequences of impulses run all over the signal: the two exist due to the ball changing (and load redistribution or varying compliance) phenomenon, while the third occurs due to the defect. Moreover, these impulses can be seen to repeat at OR fault frequency (f_{OR}). Also, it is interesting to note that the acceleration response caused by the impulses due to the defect and that due varying compliance have comparable magnitude. Hence, it is possible that even a healthy bearing manifests vibration spectra, containing OR defect frequencies of nearly identical strength as that actually produced by the defective bearings with OR defect at initial stage. This could mislead fault recognition even when the bearing has developed no fault. This misleading result has also been illustrated, experimentally in next section (Section 4.2.2).

In Fig. 16, the first impulse is excited at $t=0.0517$ s where the number of loaded balls increases from 1 to 2. The second ball remains in the load zone for longer duration, due to which the excited impulse gets sufficient time to damp out. At $t=0.0552$ s, the ball

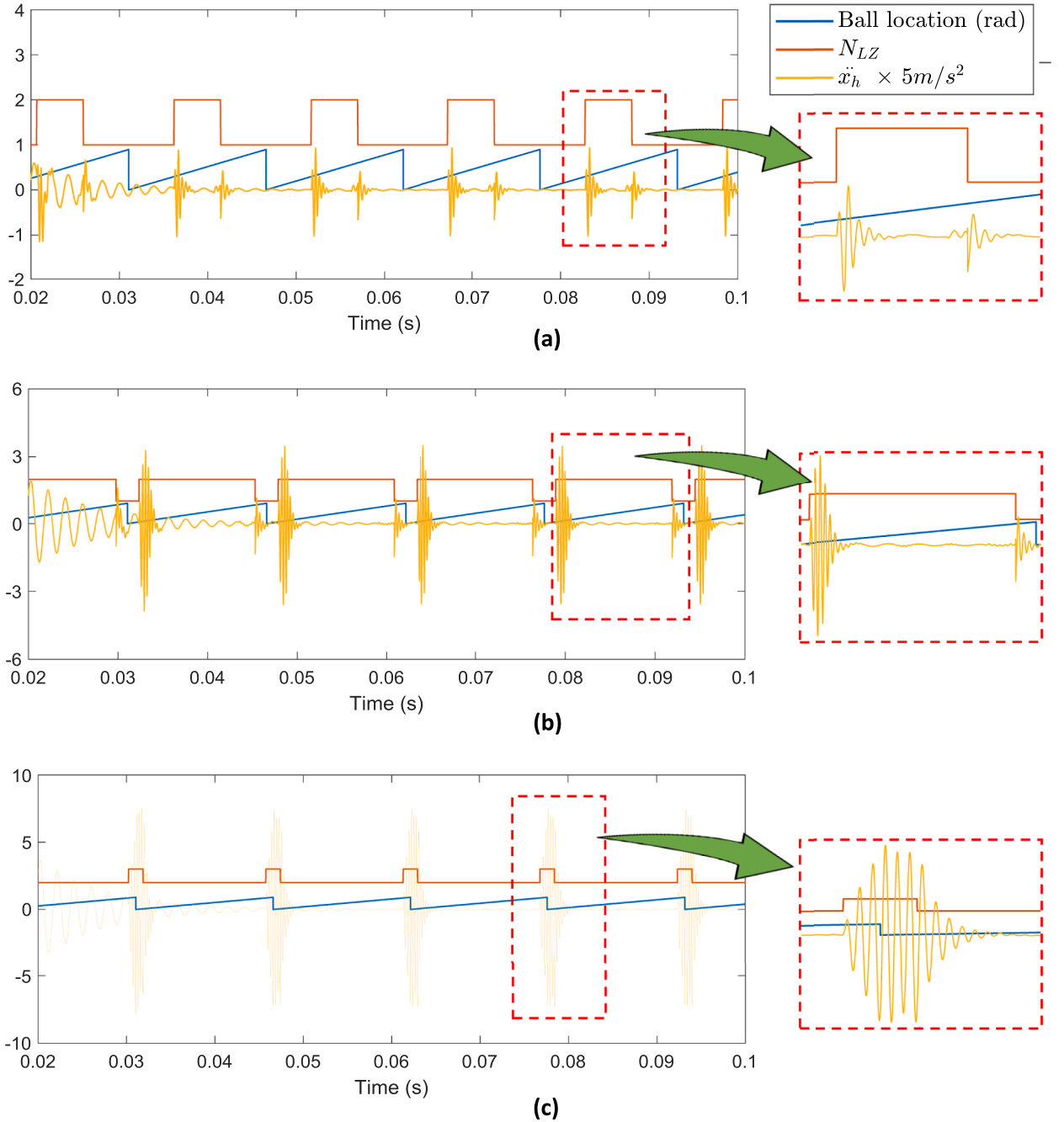


Fig. 12. Healthy bearing response at $N_s = 1500$ rpm and under (a) $F_r = 100$ N; (b) $F_r = 500$ N and; (c) $F_r = 1000$ N.

encounters the defect entry edge, where the load redistribution between the loaded balls begins, resulting in another small spike, until the ball reaches the center of the defect at $t = 0.0556$ s. At this point of time, an impulse force is generated due to striking of the ball with the trailing edge of the defect. A small lag between the impact and the acceleration spike can also be seen, which represents a system response time to the excitation. Further, the location of the fault and the combination of load and speed values are such that the defect induced impulse is so localized in time domain that it gets merged with the impulse due to load redistribution when the number of balls (N_{LZ}) in the load zone changes from two to one. This causes superposition of the two impulses which alters the characteristic of the defect induced impulse. A deeper analysis into this peak for estimating the defect size, assuming that it is purely a manifestation of the defect, can produce incorrect information.

Figs. 17 and 18 show the response of the same bearing under 500 N and 1000 N radial load, respectively. Compared to Fig. 16, the three peaks due to the three events (increasing N_{LZ} , defect, and decreasing N_{LZ}) are distinctly separated in Fig. 17, whereas in Fig. 18,

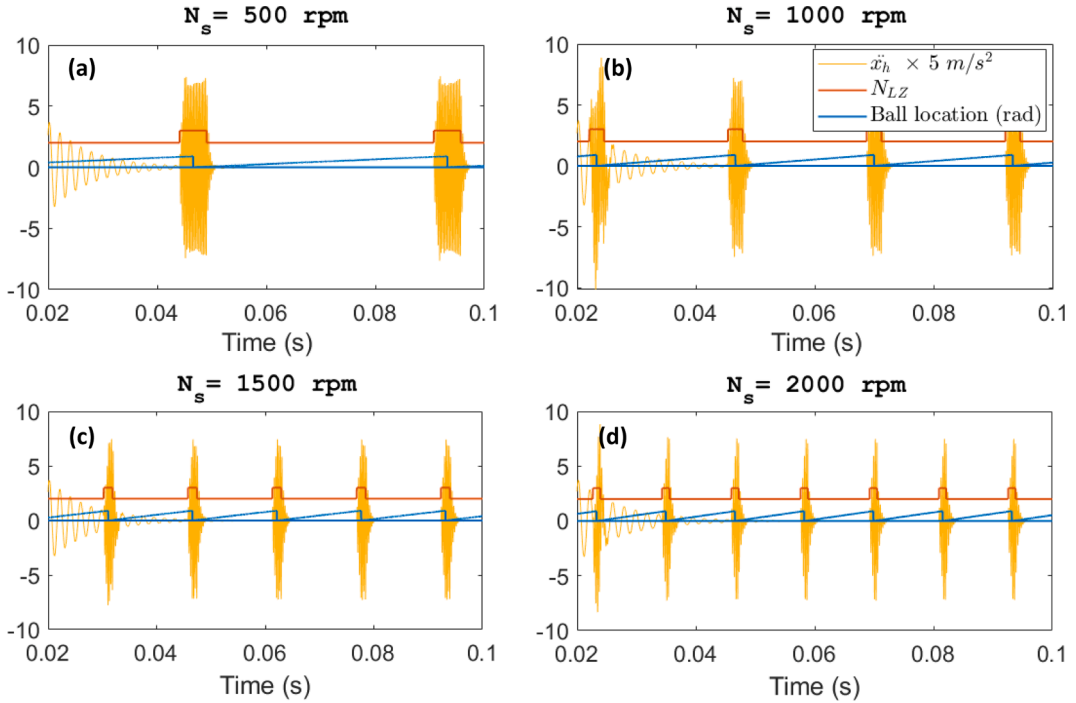


Fig. 13. Healthy bearing response under $F_r=1000$ N and at different shaft speeds, N_s (a) 500 rpm, (b) 1000 rpm, (c) 1500 rpm, and (d) 2000 rpm.

Table 2
Defect parameters.

Angular location of defect, α (deg)	30
Length of defect, a_d (mm)	1
Depth of defect, h_d (mm)	$> h_{d,crit}$
Radius of defect edge, r_d (mm)	0.01

the two peaks due to varying compliance are sufficiently close to superpose each other. Nevertheless, in both these figures, the defect impulses occur far later than the impulse due to increasing N_{LZ} is damped out. Thus, these peaks predominantly contain defect related information, and the post analysis of these peaks may provide sufficiently accurate estimate of the defect size.

Now in order to understand the effect of defect location, the vibration response of the bearing was simulated by changing α_d from 30° to 1.9°, while keeping rest of the conditions same as for Fig. 16, and the response so obtained has been plotted in Fig. 19.

For the response behavior of the bearing with defect at 1.9°, two salient observations were made with respect to the waveform of Fig. 16:

- 1 The defect peak is highly distinctive from the rest two peaks (due to varying compliance), and
- 2 The strength of defect induced peak is nearly thrice that due to fault at 1.9 deg, which is an interesting observation. It is so because in Fig. 16, the defect induced impulse occur when there are two balls in the load zone whereas the defect in case of Fig. 19 is so located that the defect impulse arises when the load zone has the least number of balls (viz one in this case). When larger number of balls share the load, each ball makes small Hertzian contact, and shift from smaller contact to the defect edge is not large which produces only small impacts. On the other hand, when lesser number of balls take up the load, the ball-raceway contact spreads over a large area and the sudden change to small contact at the exit edge of the defect give rise to strong impulse. This explains how the location of defect also play a leading role in determining the overall vibration behavior of the bearing.

From the foregoing investigation, the following inferences can be drawn:

- 1 The dual impulses in the signal waveform do not necessarily imply the entry and exit induced events. Hence, estimation of defect size based on such impulses can lead to incorrect results.
- 2 The location of impulses and the duration between consecutive impulses in the waveform are strongly governed by the bearing geometry, magnitude of applied load and the rotational speed of shaft.

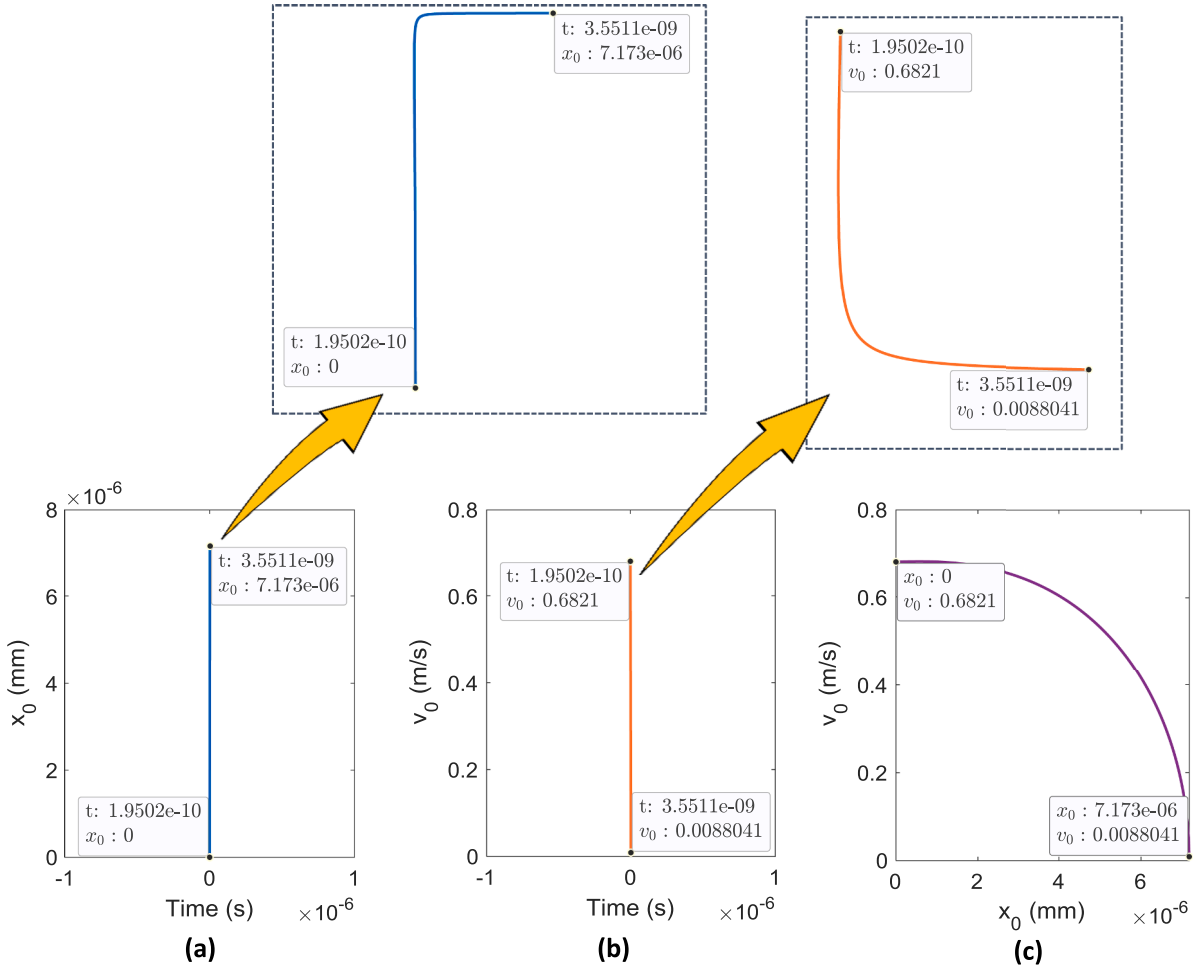


Fig. 14. Kinematics of the ball striking the trailing edge of the defect at $N_s=1500$ rpm and $F_r=1000$ N (a) deflection plot (b) velocity plot, (c) impact velocity versus deflection plot.

- 3 Impulse phenomenon due to the impact of the ball at the trailing edge is extremely short lasting, and hence, the impact force exists only for a very small duration.
- 4 Due to extremely short-lasting impulse phenomenon, precise localization of event-based impulses on waveform demands data with high sampling rate. According to the present simulation study, it was found that the sampling rate as high as 2 MHz would be required to precisely locate these events in the waveform.

It is thus conclusive from this section that the interpretations made merely on the basis of frequency spectra, or even the waveform when the impulses due to multiple events coexist (or merge, depending on the location of the defect, shaft speed and the applied load), are susceptible to unacceptable errors.

4. Experimental results and discussion

4.1. Description of the test setup

The experiments were performed on a bearing test rig as shown in Fig. 20. Before installing the test bearing on the overhanging end of the shaft, it was lubricated with lithium based grease of NLGI-2 grade, as recommended in the manufacturer's catalogue. The lubrication ensures that the test bearing operates under EHL regime. The other end of the shaft is connected to an AC motor through a flexible coupling, for receiving the driving torque. The shaft is supported over two deep groove ball bearings, placed in tandem at a small gap, and this construction provides the shaft a nearly rigid support. The motor and the support bearings are mounted onto the base plate, which in turn are placed over a concrete platform. The rubber mounts are kept beneath the base plate to isolate floor vibration from the setup. A dedicated load arm is designed to apply radial load on top of the test bearing using disc shaped dead weights of desirable value. The load arm end over the test bearing contains a slot for placement of accelerometer directly on the OR of

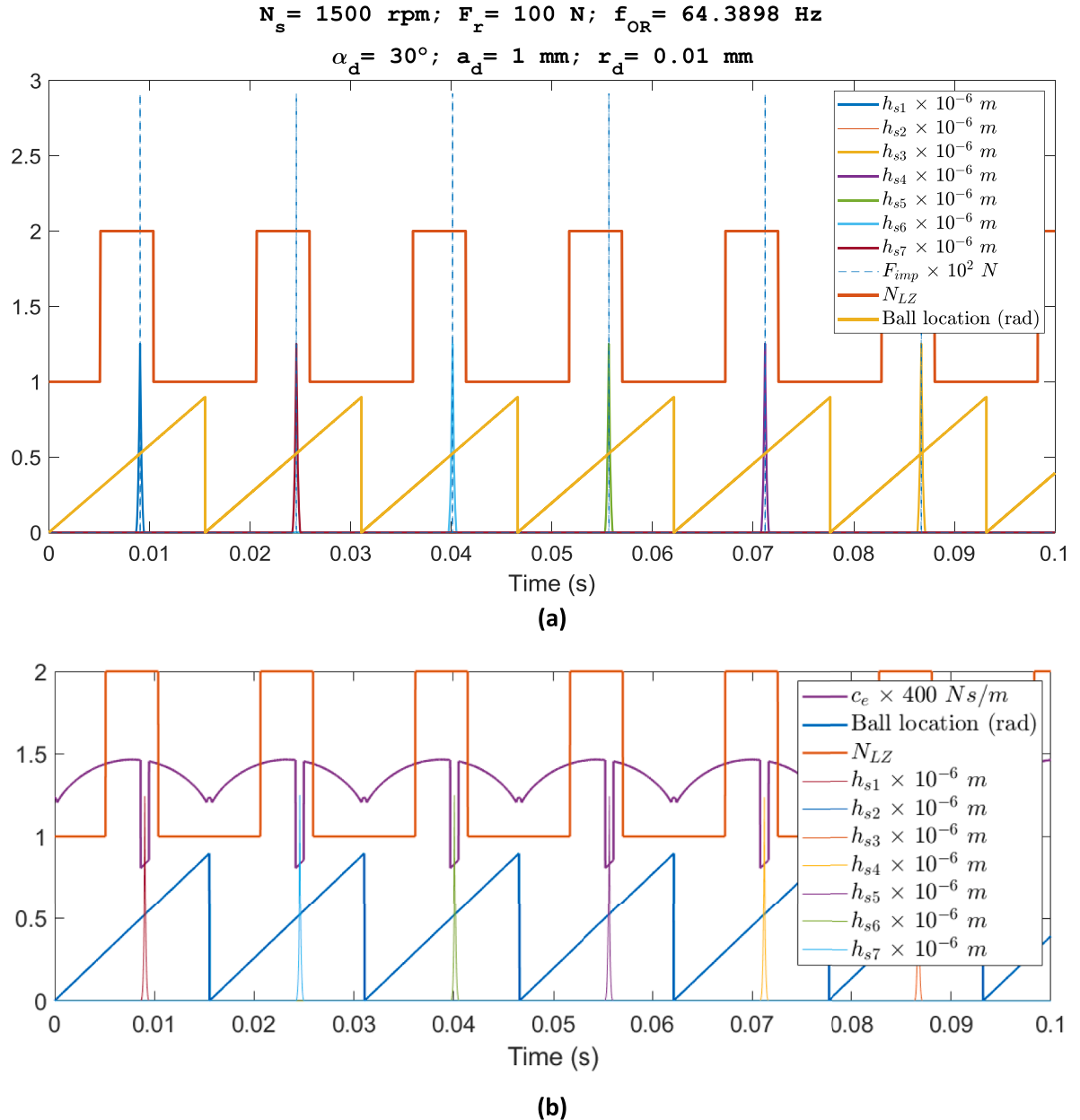


Fig. 15. Change in configuration of defective bearings with time (a) N_{LZ} , h_s and F_{imp} (b) squeezed film damping.

the test bearing. For acquiring vibration signal, a uniaxial, shear type, IEPE accelerometer (PCB 353B01) was used along with a 2-channel NI-9250 DAQ.

For validating the simulation results, a single row deep groove ball bearing (SKF-BB1B420204) with a polymeric cage was used. The data from the accelerometer was collected at 640 Hz sampling rate using MATLAB Data Acquisition tool. Experiments were conducted both on the healthy and the defective test bearings. Circular defects of 0.5 mm depth, as shown in Fig. 21, were artificially seeded on the outer races using electric discharge machining. Four different sizes of the defect were selected for study, as: 0.5 mm, 1 mm, 1.5 mm and 2 mm. These sizes are sufficiently smaller to cause single impact events for the selected test bearing.

The outer ring of the bearing was force-fit inside the housing and the IR was rotated at 1500 rpm under the application of pure radial load of about 100 N. The dynamic parameters of bearing rotor system used in the numerical calculations at these operational parameters have been already mentioned in Table 1. The outer race ball pass frequency, and its harmonics, for the selected bearing, at the selected shaft speed are also provided in this table. Since the data was collected at sampling rate of 640 Hz, the peaks could be observed only up to fourth harmonic of the outer race defect frequency, f_{OR} (viz. 257.5 Hz) in accordance with the Shannon Nyquist's sampling theorem .

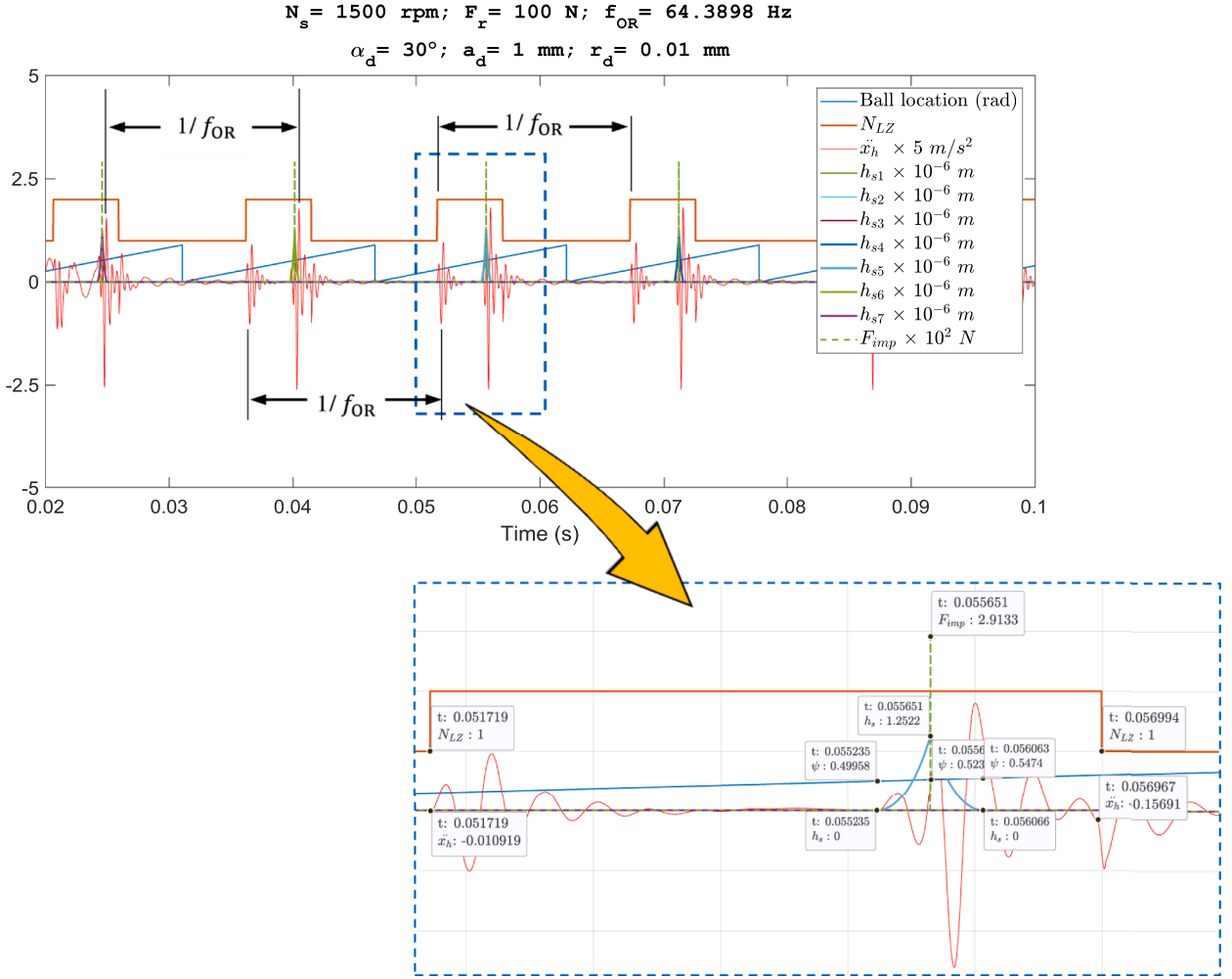


Fig. 16. Defective bearing response at $N_s=1500$ rpm and under $F_r=100$ N.

4.2. Experimental test results

4.2.1. Case I: Healthy bearing

Fig. 22 shows the frequency spectra of healthy bearing obtained using numerical simulation and experimental results.

It can be seen that even in healthy bearings, the peaks of considerable magnitude at OR defect frequency as well as its harmonics exist in both the spectra. Moreover, the peaks at shaft frequency and its harmonics are predominantly visible in experimental spectrum, however, the same are missing in simulated results because the factors causing this, like unbalance and misalignment, have not been considered in the proposed theoretical model, and only the mechanisms related to varying compliance and bearing defect have been emphasized. Further, as the sampling frequency is 640 Hz, the experimental signal contains the frequency information up to 320 Hz only (Shannon Nyquist's theorem) and hence the fifth harmonic of the defect is observed in simulated signal but not in experimental signal.

It can also be seen that there is no obvious pattern in the spectral peaks at different characteristic frequencies and their respective harmonics, both in simulated and measured results. Some defect harmonics of the simulated response are stronger than that of measured response, while others are weaker. Nonetheless, it is also evident that the defect peaks in both the plots spans over the same scale and the values of the peaks are approximately same in numerical and experimental plots. The small difference between the amplitudes of experimental and numerical results is mainly due to the inaccuracies associated with the calculated values of structural damping, material and contact stiffnesses, and oil film thickness (and hence squeezed film damping), and difference between the actual and assumed values of defect edge radius. Other contributing factors include the assumptions listed in Section 2.2, like looseness between bearing and housing components, different bearing clearance from that considered in the numerical simulation. This causes excitations, stronger than predicted, every time the defect is encountered by the ball. Another reason for the difference between the experimental and the predicted values lies in the fact that the presence of non-ideal conditions, like unbalance and misalignment, which were not considered in the simulation. This influences the spectral energy distribution and alters the magnitude of the defect

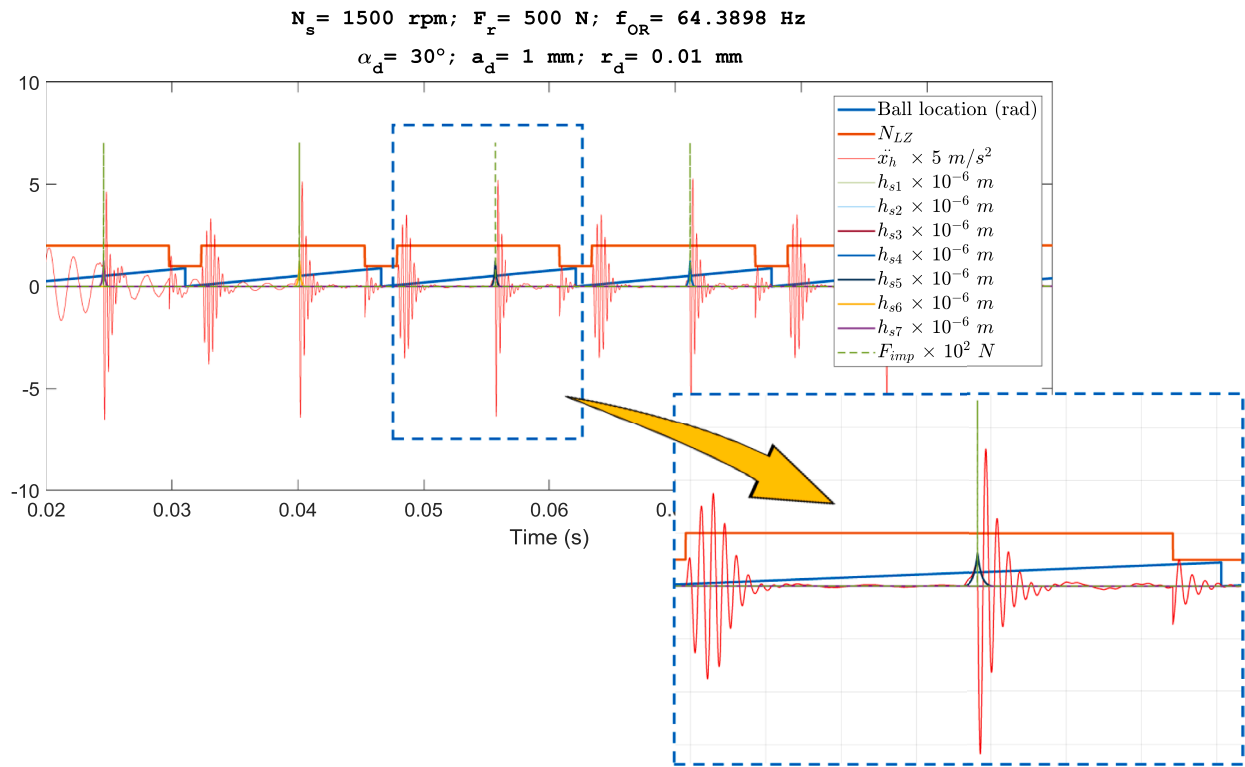


Fig. 17. Defective bearing response at $N_s=1500 \text{ rpm}$ and under $F_r=500 \text{ N}$.

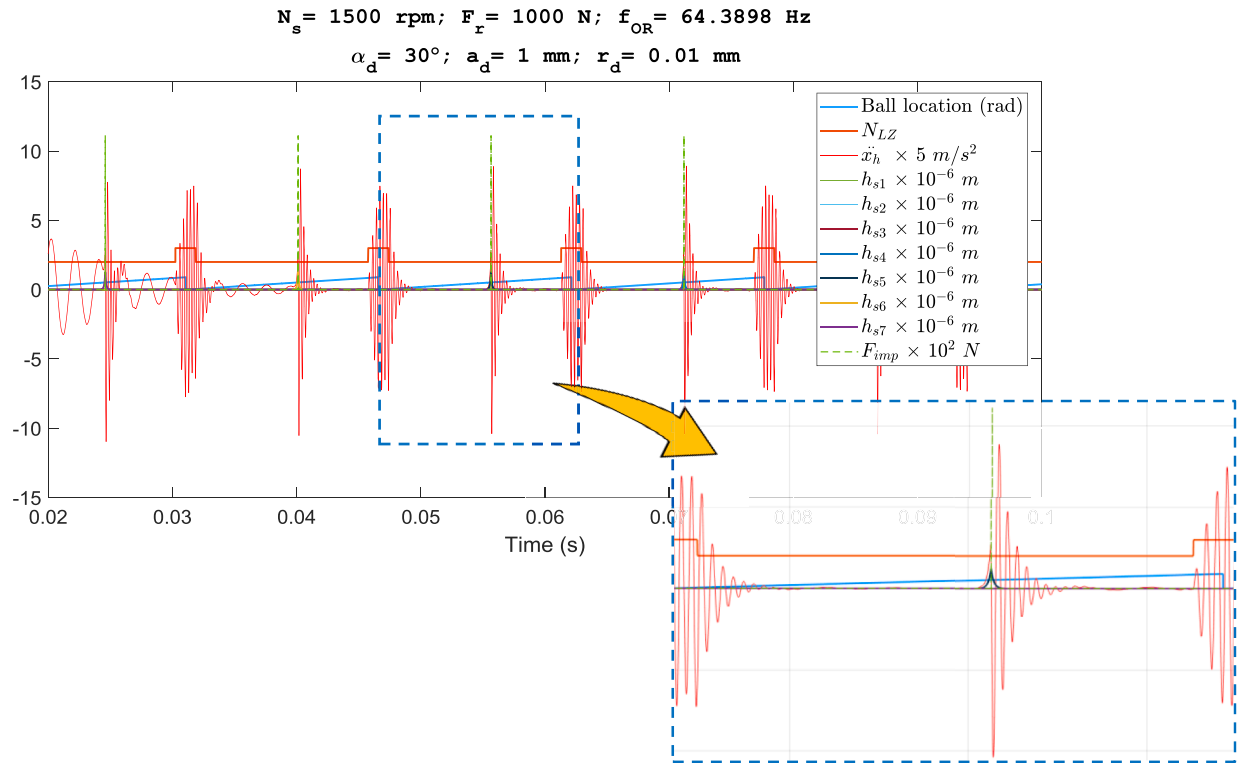


Fig. 18. Defective bearing response at $N_s=1500 \text{ rpm}$ and under $F_r=1000 \text{ N}$.

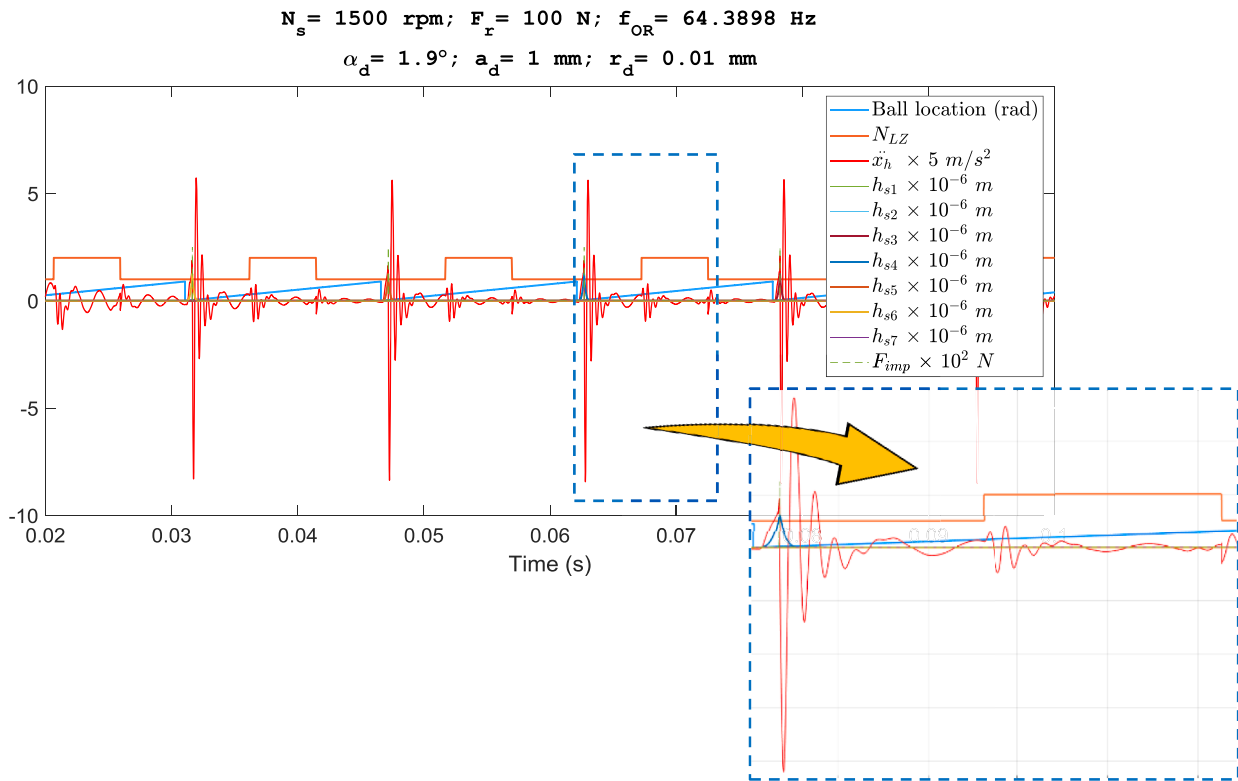


Fig. 19. Response waveform of defective bearing at $N_s=1500$ rpm and under $F_r=100$ N with defect located at 1.9° from load line.

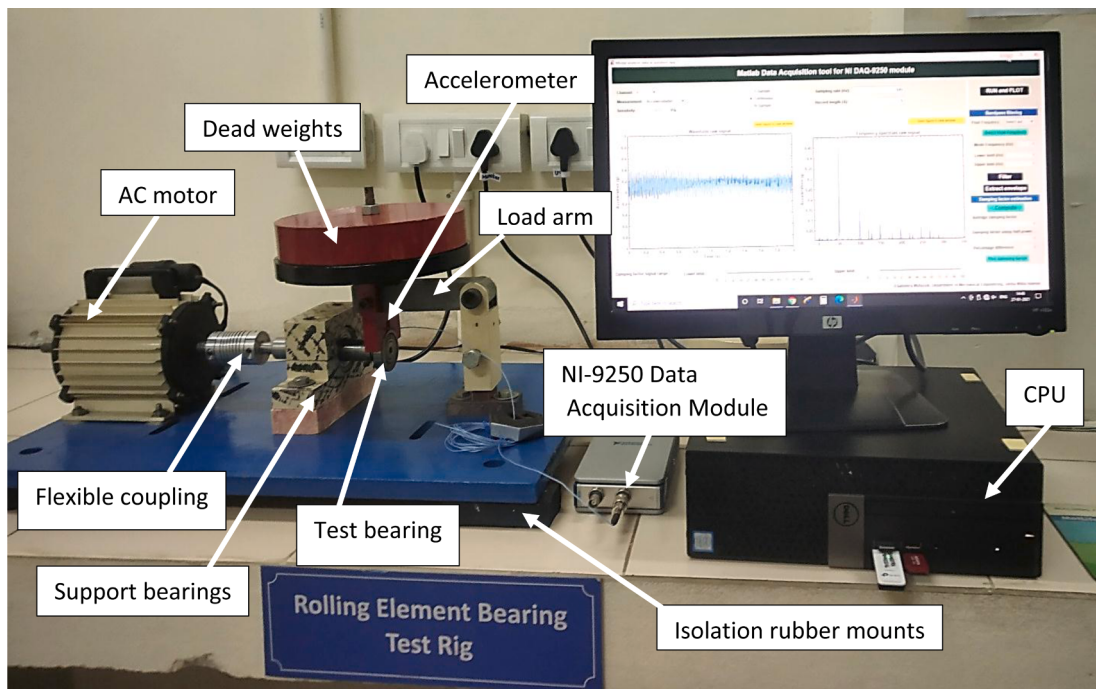


Fig. 20. Experimental test rig for ball bearing fault diagnosis.



Fig. 21. Circular defect on OR of the test bearing.

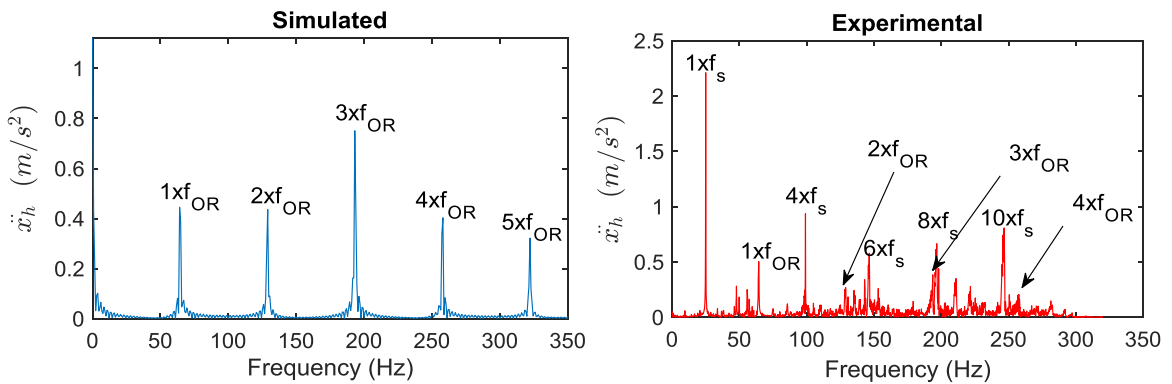


Fig. 22. Frequency spectra of simulated and real signals for healthy bearing at $N_s=1500$ rpm and under $F_r=100$ N.

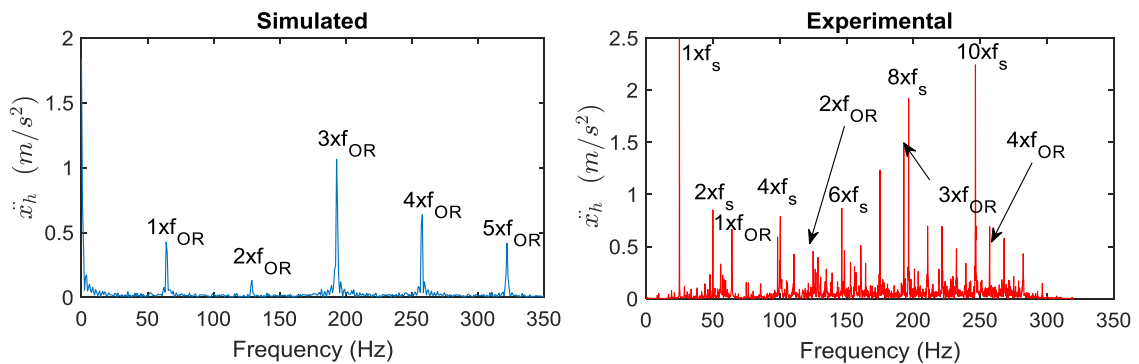


Fig. 23. Frequency spectra of simulated and real signals for defective bearing with $a_d = 0.5$ mm at $N_s=1500$ rpm and under $F_r=100$ N.

induced vibration peaks.

4.2.2. Case II: Defective bearing

The frequency spectra of defective bearings with all the four defect sizes have been plotted in Figs. 23–26. When compared to healthy bearing results, it can be seen that the scale of defect induced peaks has increased in both the simulated and experimental plots. While moving from plots of small defect to larger size defects, i.e. Figs. 23–26, it is noticed that the defect induced peaks rise at increasing rate. On the same hand, it is also interesting to note that as the defect arises in the bearing, the shaft harmonics become more dominant, which indicates that the arrival of defect in the bearing affects the overall energy distribution of the spectrum, and thus the magnitude of peaks due to unbalance and misalignment also gets altered. Nevertheless, the impact on defect induced frequency is relatively higher than that on shaft related frequencies.

Figs. 23–26 also reveal that as the defect size increases from 0.5 mm to 2 mm, the variation between the spectral peaks' magnitudes at different defect harmonics become less distinguished in case of simulated spectrum, while this is not true in case of experimental

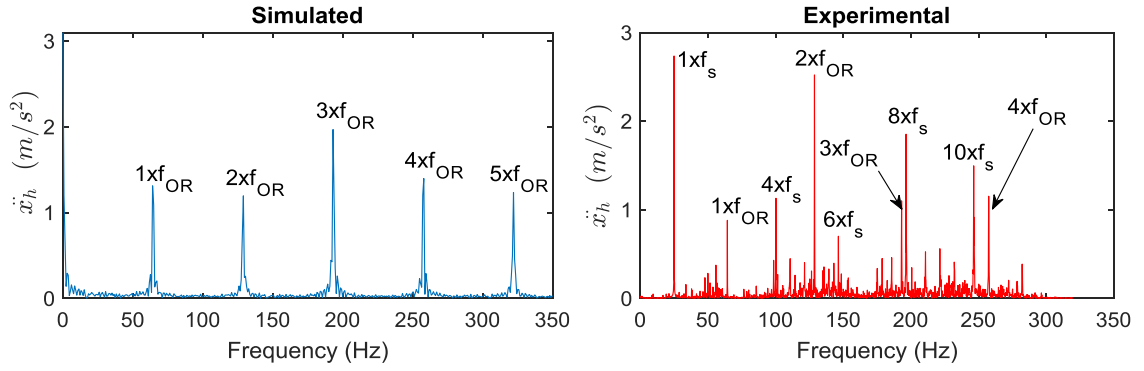


Fig. 24. Frequency spectra of simulated and real signals for defective bearing with $a_d = 1$ mm at $N_s=1500$ rpm and under $F_r=100$ N.

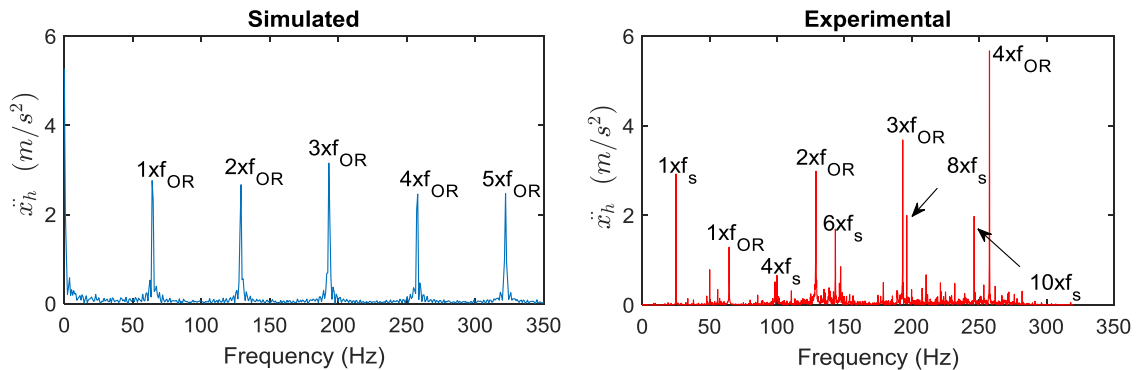


Fig. 25. Frequency spectra of simulated and real signals for defective bearing with $a_d = 1.5$ mm at $N_s=1500$ rpm and under $F_r=100$ N.

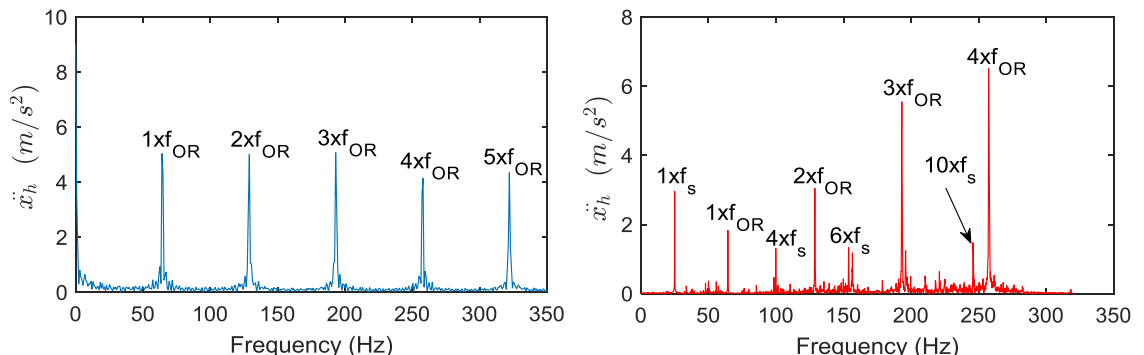


Fig. 26. Frequency spectra of simulated and real signals for defective bearing with $a_d = 2$ mm at $N_s=1500$ rpm and under $F_r=100$ N

spectrum. But for large sized defect (1.5 mm and 2 mm), the strength of peaks increases with defect harmonics in case of experimental results. The relative strength of the defect induced peaks are illustrated in Fig. 27.

It can be observed that the defect has unequal impact on the magnitude of different harmonics, e.g., unlike other harmonics, the second harmonic of the BPFO is smaller in simulated spectrum of defective bearing with $a_d=0.5$ mm than that of healthy bearing. Similar observations can be made for experimental data corresponding to the third harmonic where the defect size increases from 0.5 mm to 1.00 mm. This indicates that as the defect appears in the bearing, the overall spectral energy is redistributed and becomes concentrated at the defect induced peaks, thereby making them stronger. However, the redistribution does not necessarily have equally increasing effect on each harmonic. Further, it will be interesting to note from the comparative results that as the defect size increases, the deviation between the predicted and actual magnitude of spectral peaks grows, which indicates that the proposed model is highly suitable for newly generated spalls, especially for defect size up to 0.5 mm for the presented case.

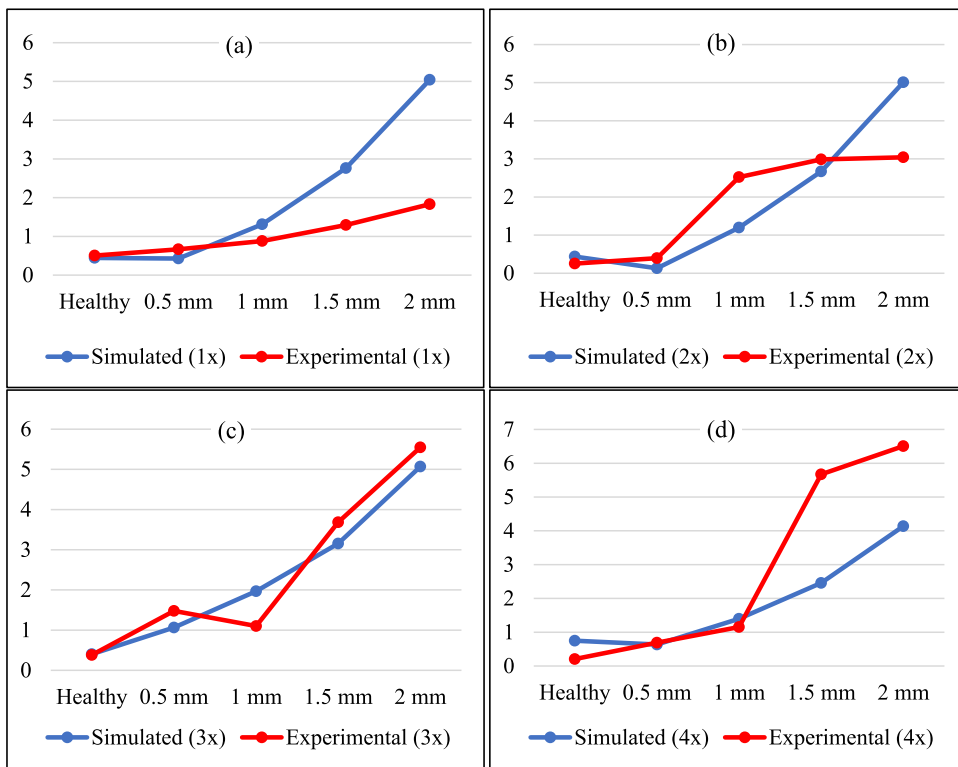


Fig. 27. A comparative view of simulated and experimental values of acceleration peaks (in ms^{-2}) at OR defect frequency and its a) first (1X), (b) second (2X), (c) third (3X), and (d) fourth (4X) harmonics.

5. Conclusion

A detailed analysis of rolling element bearing vibration with OR defect has been conducted and it has been demonstrated that the response of healthy bearing and defective bearing with small size defect is highly similar from viewpoint of the impulse strength in waveform and magnitude of peaks at OR defect frequency and its harmonics. It is thus established that although the variation in stiffness due to orbital motion of the balls and cage assembly could be small, as reported in earlier research work, but the strength of the resulting vibration peaks at OR defect frequency, and its subsequent harmonics, cannot be overlooked. The ignorance of varying compliance vibration, and OR fault prediction merely based on spectrum analysis, followed by fault size estimation from the knowledge of dual impulse peaks in time waveform do not suffice the precise bearing health monitoring. It is found that the location of the impulses in the waveform signal is influenced by multiple factors, predominantly, the values of applied load and shaft rotational speed, and the angular location of OR defect (for defective bearing). Variation in the values of these parameters can cause either superposition or separation of the impulses and hence, the signal waveforms will not necessarily contain dual impulse sequences. It is finally discovered that in order to confidently predict the presence of OR fault, it is also important to have the complete acquaintance with actual load acting over the bearing as well as the IR speed. This will help in accurate localization of impulse peaks, and finally identify the source of the impulses (i.e. either due to varying compliance or because of the defect) before conducting the fault diagnosis on the ground of these peaks. However, the precise measurement of load acting on the bearing will pose another big challenge towards fault diagnosis, which apparently is a limitation of the present research. This forms the motivation for the future research work, in addition to experimentally investigate the effects of load on the waveform both in healthy and defective bearing and then to correlate the results with those of the proposed theoretical model.

Authors credit

Sameera Mufazzal: Conceptualization, Mathematical Computations, Writing- Original draft

S. M. Muzakkir: Supervision, Visualization, Writing-Review and Editing

Sidra Khanam: Supervision, Validation, Writing-Review and Editing

Declaration of Competing Interest

The authors declare that they have no known competing financial interests or personal relationships that could have appeared to

influence the work reported in this paper.

Acknowledgment

The first author of this manuscript acknowledges the financial assistance of Department of Science & Technology (DST)-India, in terms of Junior Research Fellowship (JRF)-INSPIRE for supporting this research.

References

- [1] H. Cao, L. Niu, S. Xi, X. Chen, Mechanical model development of rolling bearing-rotor systems: a review, *Mech. Syst. Signal Process.* 102 (2018) 37–58, <https://doi.org/10.1016/j.ymssp.2017.09.023>.
- [2] J. Liu, C. Tang, H. Wu, Z. Xu, L. Wang, An analytical calculation method of the load distribution and stiffness of an angular contact ball bearing, *Mech. Mach. Theory* 142 (2019), 103597, <https://doi.org/10.1016/j.mechmachtheory.2019.103597>.
- [3] D.S. Shah, V.N. Patel, A review of dynamic modeling and fault identifications methods for rolling element bearing, *Proc. Technol.* (2014) 447–456, <https://doi.org/10.1016/j.protcy.2014.08.057>.
- [4] P.D. McFadden, J.D. Smith, Model for the vibration produced by a single point defect in a rolling element bearing, *J. Sound Vib.* 96 (1984) 69–82, [https://doi.org/10.1016/0022-460X\(84\)90595-9](https://doi.org/10.1016/0022-460X(84)90595-9).
- [5] P.D. McFadden, J.D. Smith, The vibration produced by multiple point defects in a rolling element bearing, *J. Sound Vib.* 98 (1985) 263–273, [https://doi.org/10.1016/0022-460X\(85\)90390-6](https://doi.org/10.1016/0022-460X(85)90390-6).
- [6] I.K. Epps, *An Investigation into Vibrations by Faults in Rolling Element Bearings*, University of Canterbury, Christchurch, New Zealand, 1991.
- [7] N. Sawalhi, R.B. Randall, Simulating gear and bearing interactions in the presence of faults. Part I. The combined gear bearing dynamic model and the simulation of localised bearing faults, *Mech. Syst. Signal Process.* 22 (2008) 1924–1951, <https://doi.org/10.1016/j.ymssp.2007.12.001>.
- [8] L. Niu, H. Cao, Z. He, Y. Li, Dynamic modeling and vibration response simulation for high speed rolling ball bearings with localized surface defects in raceways, *J. Manuf. Sci. Eng. Trans. ASME* 136 (2014) 1–16, <https://doi.org/10.1115/1.4027334>.
- [9] S. Singh, U.G. Körpe, C.Q. Howard, D. Petersen, Analyses of contact forces and vibration response for a defective rolling element bearing using an explicit dynamics finite element model, *J. Sound Vib.* 333 (2014) 5356–5377, <https://doi.org/10.1016/j.jsv.2014.05.011>.
- [10] N. Tandon, A. Choudhury, An analytical model for the prediction of the vibration response of rolling element bearings due to localized defect, *J. Sound Vib.* 205 (1997) 275–292, [https://doi.org/10.1016/0011-2240\(79\)90049-X](https://doi.org/10.1016/0011-2240(79)90049-X).
- [11] J. Sopanen, A. Mikkola, Dynamic model of a deep-groove ball bearing including localized and distributed defects. Part 1: theory, *Proc. Inst. Mech. Eng. Part K J. Multi-Body Dyn.* 217 (2003) 201–211, <https://doi.org/10.1243/14644190360713551>.
- [12] D. Brie, Modelling of the spalled rolling element bearing vibration signal: an overview and some new results, *Mech. Syst. Signal Process.* 14 (2000) 353–369, <https://doi.org/10.1006/mssp.1999.1237>.
- [13] A. Rafsanjani, S. Abbasiyan, A. Farshidianfar, H. Moeenfar, Nonlinear dynamic modeling of surface defects in rolling element bearing systems, *J. Sound Vib.* 319 (2009) 1150–1174, <https://doi.org/10.1016/j.jsv.2008.06.043>.
- [14] A. Moazen Ahmadi, D. Petersen, C. Howard, A nonlinear dynamic vibration model of defective bearings - The importance of modelling the finite size of rolling elements, *Mech. Syst. Signal Process.* 52–53 (2015) 309–326, <https://doi.org/10.1016/j.ymssp.2014.06.006>.
- [15] A. Ashtekar, F. Sadeghi, L.E. Stacke, A new approach to modeling surface defects in bearing dynamics simulations, *J. Tribol.* 130 (2008) 1–8, <https://doi.org/10.1115/1.2959106>.
- [16] A. Choudhury, N. Tandon, Vibration response of rolling element bearings in a rotor bearing system to a local defect under radial load, *J. Tribol.* 128 (2006) 252–261, <https://doi.org/10.1115/1.2164467>.
- [17] V.N. Patel, N. Tandon, R.K. Pandey, A dynamic model for vibration studies of deep groove ball bearings considering single and multiple defects in races, *J. Tribol.* 132 (2010), <https://doi.org/10.1115/1.4002333>.
- [18] D.S. Shah, V.N. Patel, A dynamic model for vibration studies of dry and lubricated deep groove ball bearings considering local defects on races, *Meas. J. Int. Meas. Confed.* 137 (2019) 535–555, <https://doi.org/10.1016/j.measurement.2019.01.097>.
- [19] M.S. Patil, J. Mathew, P.K. Rajendrakumar, S. Desai, A theoretical model to predict the effect of localized defect on vibrations associated with ball bearing, *Int. J. Mech. Sci.* 52 (2010) 1193–1201, <https://doi.org/10.1016/j.ijmecsci.2010.05.005>.
- [20] A.P. Patil, B.K. Mishra, S.P. Harsha, Vibration based modelling of acoustic emission of rolling element bearings, *J. Sound Vib.* 468 (2020), 115117, <https://doi.org/10.1016/j.jsv.2019.115117>.
- [21] D. Petersen, C. Howard, N. Sawalhi, A. Moazen Ahmadi, S. Singh, Analysis of bearing stiffness variations, contact forces and vibrations in radially loaded double row rolling element bearings with raceway defects, *Mech. Syst. Signal Process.* 50–51 (2015) 139–160, <https://doi.org/10.1016/j.ymssp.2014.04.014>.
- [22] J. Liu, A dynamic modelling method of a rotor-roller bearing-housing system with a localized fault including the additional excitation zone, *J. Sound Vib.* 469 (2020), 115144, <https://doi.org/10.1016/j.jsv.2019.115144>.
- [23] L. Niu, H. Cao, Z. He, Y. Li, A systematic study of ball passing frequencies based on dynamic modeling of rolling ball bearings with localized surface defects, *J. Sound Vib.* 357 (2015) 207–232, <https://doi.org/10.1016/j.jsv.2015.08.002>.
- [24] L. Niu, H. Cao, X. Xiong, Dynamic modeling and vibration response simulations of angular contact ball bearings with ball defects considering the three-dimensional motion of balls, *Tribol. Int.* 109 (2017) 26–39, <https://doi.org/10.1016/j.triboint.2016.12.011>.
- [25] L. Niu, F. Wang, G. Li, C. Niu, Y. Lan, X. Xiong, Calculating the contact forces at imperfect surfaces considering elastohydrodynamic lubrication effects in rolling element bearings, in: 2019 IEEE International Conference on Prognostics and Health Management ICPHM 2019, 2019, pp. 1–6, <https://doi.org/10.1109/ICPHM.2019.8819428>.
- [26] J. Liu, Y. Shao, T.C. Lim, Vibration analysis of ball bearings with a localized defect applying piecewise response function, *Mech. Mach. Theory* 56 (2012) 156–169, <https://doi.org/10.1016/j.mechmachtheory.2012.05.008>.
- [27] J. Liu, Y. Shao, W.D. Zhu, A new model for the relationship between vibration characteristics caused by the time-varying contact stiffness of a deep groove ball bearing and defect sizes, *J. Tribol.* 137 (2015) 1–15, <https://doi.org/10.1115/1.4029461>.
- [28] J. Liu, Y. Shao, A new dynamic model for vibration analysis of a ball bearing due to a localized surface defect considering edge topographies, *Nonlinear Dyn.* 79 (2015) 1329–1351, <https://doi.org/10.1007/s11071-014-1745-y>.
- [29] Y. Shao, J. Liu, J. Ye, A new method to model a localized surface defect in a cylindrical roller-bearing dynamic simulation, *Proc. Inst. Mech. Eng. Part J J. Eng. Tribol.* 228 (2014) 140–159, <https://doi.org/10.1177/1350650113499745>.
- [30] F. Wang, M. Jing, J. Yi, G. Dong, H. Liu, B. Ji, Dynamic modelling for vibration analysis of a cylindrical roller bearing due to localized defects on raceways, *Proc. Inst. Mech. Eng. Part K J. Multi-Body Dyn.* 229 (2015) 39–64, <https://doi.org/10.1177/1464419314546539>.
- [31] X. Yuan, Y.S. Zhu, Y.Y. Zhang, Multi-body vibration modelling of ball bearing-rotor system considering single and compound multi-defects, *Proc. Inst. Mech. Eng. Part K J. Multi-Body Dyn.* 228 (2014) 199–212, <https://doi.org/10.1177/1464419314522372>.
- [32] J. Kang, Y. Lu, Y. Zhang, C. Liu, S. Li, N. Müller, Investigation on the skidding dynamic response of rolling bearing with local defect under elastohydrodynamic lubrication, *Mechanics & Industry* 20 (2019) 1–33, <https://doi.org/10.1051/meca/2019054>, 615 In this issue.
- [33] Y. Qin, C. Li, X. Wu, Y. Wang, H. Chen, Multiple-degree-of-freedom dynamic model of rolling bearing with a localized surface defect, *Mech. Mach. Theory* 154 (2020), 104047, <https://doi.org/10.1016/j.mechmachtheory.2020.104047>.
- [34] J. Liu, Y. Xu, G. Pan, A combined acoustic and dynamic model of a defective ball bearing, *J. Sound Vib.* 501 (2021), 116029, <https://doi.org/10.1016/j.jsv.2021.116029>.

- [35] Y. Yang, W. Yang, D. Jiang, Simulation and experimental analysis of rolling element bearing fault in rotor-bearing-casing system, Eng. Fail. Anal. 92 (2018) 205–221, <https://doi.org/10.1016/j.engfailanal.2018.04.053>.
- [36] S. Sassi, B. Badri, M. Thomas, A numerical model to predict damaged bearing vibrations, JVC/J. Vib. Control. 13 (2007) 1603–1628, <https://doi.org/10.1177/1077546307080040>.
- [37] C. Mishra, A.K. Samantaray, G. Chakraborty, Bond graph modeling and experimental verification of a novel scheme for fault diagnosis of rolling element bearings in special operating conditions, J. Sound Vib. 377 (2016) 302–330, <https://doi.org/10.1016/j.jsv.2016.05.021>.
- [38] H. Cao, L. Niu, Z. He, Method for vibration response simulation and sensor placement optimization of a machine tool spindle system with a bearing defect, Sensors (Switzerland) 12 (2012) 8732–8754, <https://doi.org/10.3390/s120708732>.
- [39] D. Gazizulin, L. Rosado, R. Schneck, R. Klein, J. Bortman, A new efficient rolling element – Spall edge interaction model, Int. J. Fatigue 131 (2020), 105330, <https://doi.org/10.1016/j.ijfatigue.2019.105330>.
- [40] S. Khanam, N. Tandon, J. Dutt, Multi-event excitation force model for inner race defect in a rolling element bearing, J. Tribol. ASME. 138 (2016), <https://doi.org/10.1115/1.4031394>.
- [41] S. Khanam, J.K. Dutt, N. Tandon, Impact force based model for bearing local fault identification, J. Vib. Acoust. 137 (2016) 1–13, <https://doi.org/10.1115/1.4029988>.
- [42] M. Singh, R.K. Yadav, R. Kumar, Discrete wavelet transform based measurement of inner race defect width in taper roller bearing, MAPAN-J. Metrol. Soc. India 28 (2013) 17–23, <https://doi.org/10.1007/s12647-013-0045-1>.
- [43] M. Singh, R. Kumar, Thrust bearing groove race defect measurement by wavelet decomposition of pre-processed vibration signal, Meas. J. Int. Meas. Confed. 46 (2013) 3508–3515, <https://doi.org/10.1016/j.measurement.2013.06.044>.
- [44] S. Khanam, N. Tandon, J.K. Dutt, Fault size estimation in the outer race of ball bearing using discrete wavelet transform of the vibration signal, Proc. Technol. 14 (2014) 12–19, <https://doi.org/10.1016/j.protcy.2014.08.003>.
- [45] R. Kumar, M. Singh, Outer race defect width measurement in taper roller bearing using discrete wavelet transform of vibration signal, Meas. J. Int. Meas. Confed. 46 (2013) 537–545, <https://doi.org/10.1016/j.measurement.2012.08.012>.
- [46] M.F. White, Rolling element bearing vibration transfer characteristics: effect of stiffness, J. Appl. Mech. 46 (1979) 677–684.
- [47] C. Mishra, A.K. Samantaray, G. Chakraborty, Ball bearing defect models: a study of simulated and experimental fault signatures, J. Sound Vib. 400 (2017) 86–112, <https://doi.org/10.1016/j.jsv.2017.04.010>.
- [48] T.A. Harris, M.N. Kotzalas, Rolling Bearing Analysis: Essential concepts of bearing technology, Fifth, Taylor & Francis, 1986, https://doi.org/10.1007/978-1-4684-5116-0_1.
- [49] B.J. Hamrock, W.J. Anderson, NASA reference publication 1105, Rolling-Element Bearings, 1983.
- [50] G.D. Hagiu, M.D. Gafitatu, Dynamic characteristics of high speed angular contact ball bearings, Wear 211 (1997) 22–29.
- [51] S. Mufazzal, S.M. Muzakkir, S. Khanam, Numerical investigation of the effect of ball bearing geometry on oil film damping due to lubricated contact at different loads, in: G. Manik, S. Kalia, S.K. Sahoo, T.K. Sharma, O.P. Verma (Eds.), Advanced Mechanical Engineering CAMSE 2020, Springer, Singapore, 2021, pp. 1–305, https://doi.org/10.1007/978-981-16-0942-8_2.
- [52] H. Rahnejat, R. Gohar, The vibrations of radial ball bearings, Proc. Inst. Mech. Eng., Part I J. Syst. Control Eng. 199 (1985) 181–193, <https://doi.org/10.1243/PIME>.
- [53] A. Mostofi, R. Gohar, Oil film thickness and pressure distribution in elastohydrodynamic point contacts, Proc. Inst. Mech. Eng. Part C J. Mech. Eng. Sci. 24 (1982), <https://doi.org/10.1243/JMES>.
- [54] A. Mostofi, Oil film thickness and pressure distribution in elastohydrodynamic elliptical contacts, PhD thesis, Imperial College London, 1981.
- [55] B.J. Hamrock, D. Dowson, Isothermal elastohydrodynamic lubrication of point contacts: Part III- Fully flooded results, Am. Soc. Mech. Eng. 99 (2) (1977) 264–275, <https://doi.org/10.1115/1.3453074>.